POLITECNICO

MILANO 1863
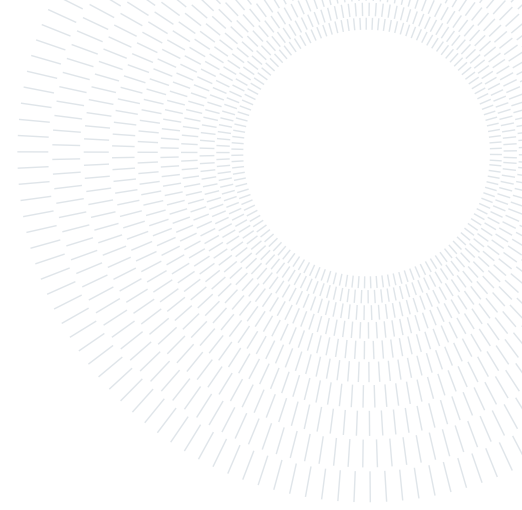
A Model for Meltwater Infiltration and Refreezing in Snow under Non-Isothermal Conditions

Tesi di Laurea Magistrale in
Mathematical Engineering - Ingegneria Matematica

Camilla Crippa, 10616381

Advisor:
Prof. Alessio Fumagalli

Co-advisors:
Prof.ssa Anna Scotti

Academic year:
2022-2023

Abstract: The flow of meltwater through snow, acknowledged as a porous medium, is a crucial hydrological process essential for predicting the cryosphere's response to climate change. This thesis aims to model the intricate coupling between meltwater infiltration and the non-equilibrium thermodynamics of ice-melt phase change at the Darcy scale. The proposed model consists of the Richards' equation for infiltration, and evolution equations for ice and water temperature fields, which account for the thermal budget resulting from melt refreezing. Additionally, the model considers variations in porosity. This study presents numerical results from simulations conducted on 2D models of snowpacks with distinct initial levels of dryness and varying physical setups, which examine the mechanics of infiltration and alteration of the porosity structure due to refreezing. The implementation employs the *PorePy* and *PyGeoN* Python libraries.

1. Introduction

Predicting the hydrological cycle in cold environments, like snowpacks and glaciers, involves significant challenges but holds primary importance for water resource management. An important yet insufficiently comprehended aspect entails the phenomenon of infiltration of surface-generated meltwater within the snowpack [18, 23, 33]. This is vital for avalanche risk assessment and glacier movement comprehension. As a matter of fact, infiltrating water can serve as a lubricant, facilitating snowpack or glacier sliding over the underlying bedrock.

The aim of this work is to develop and implement a model that explores meltwater infiltration, taking advantage of the classification of snow as a porous medium. In addressing a two-phase flow scenario where the void space concurrently includes both water and air, we can apply the *Richards' assumption* [25, 28] to the air phase. This assumption allows us to derive an equation that governs the behavior of the water phase, known as Richards' equation.

Infiltration commonly exhibits a heterogeneous nature, wherein the formation of fingers is attributed to a combination of property heterogeneities and the intrinsic instability of the meltwater front. This aspect can be modeled, as demonstrated in [23], by introducing a higher-order term into the Richards' equation. However, in this work, we intentionally overlook this aspect, concentrating solely on the fluid-dynamic/thermal coupling and consequently adopting the classical version of the equation. In thermodynamic terms, we consider non-isothermal conditions, addressing the effects of latent heat release during phase change and its impact on the

snowpack's thermal energy balance. Specifically, we adopt a dual-temperature field framework that embraces a *local thermal non-equilibrium* (LTNE) condition, where the modeling of the thermal budget is based on the framework proposed by [16]. Moreover, the model addresses variations in porosity by including a mass conservation equation for the solid matrix. Note that, in melting snow, a change in porosity corresponds to a source term in the fluid mass conservation equation as ice melts forming water.

The model is clearly multiphysics and strongly coupled. In this study, we design an iterative coupling between the two macroprocesses - fluid mechanics and thermodynamics - while we explore an implicit coupling within each individual macroprocess. Specifically, the nonlinearity in Richards' equation is addressed using the L-scheme [22], while the coupling between the two temperature fields is treated at the level of the reaction term in the advection-diffusion-reaction equations that govern them [6].

To numerically solve this system of equations, we carry out both time and space discretization for all the equations involved. Specifically, we exploit the Mixed Finite Element Method for solving Richards' equation [13], while, for the thermal budget equations, we employ the Finite Volume Method discretization scheme [9, 21, 27]. These discretization methods are specifically implemented in all their components in the Python libraries *PorePy* [19] and *PyGeoN* [11].

To start understanding the nature of the problem, we initially consider a zero-dimensional experiment with two distinct physical initial conditions. We then proceed to the two-dimensional scenario, aiming to simulate the infiltration phenomenon in a 2D domain representing a cross section of the snowpack, and comprehend the interplay between all the involved quantities. Various setups are introduced to investigate different scenarios. For each test, we conduct an analysis on the convergence of the coupling scheme.

This work is primarily structured into four sections. In Section 2, we explore the concept of a porous medium, outlining the equations that govern single-phase flow and two-phase flow. We then contextualize this concept to our specific problem by introducing Richards' equation. Section 3 concretely presents the complete coupled model associated with the discussed phenomenon, along with the pertinent equations and constitutive relationships. Subsequently, in Section 4, we progressively introduce the fully discretized versions of all the model equations, along with the general numerical setup for the simulations. The numerical results of the simulations and comments on the outcomes are then presented in Section 5. Finally, the conclusions and future developments are discussed in Section 6.

2.   Theoretical framework

It's widely known that the microscopic structure of snow consists of ice crystals, also referred to as *grains*, which, instead of occupying the entire volume, create, when packed, void spaces within the structure. Endowed with this attribute, snow can be classified as a porous medium.

In this section, we introduce the concept of a porous medium and its characteristics (see Section 2.1), in order to deepen our comprehension of the system's properties and technical terminology.

Subsequently, Section 2.2 delves into the equations governing single-phase flow, where we consider the void space of our medium filled with only one liquid or gas.

Finally, in Section 2.3, we discuss the equations related to two-phase flow, followed by the introduction of Richards' equation and its intricate characteristics. We will observe that the latter model is the most suited for the problem of our interest.

2.1.   Porous medium

A *porous medium* is a region of space characterised by the presence of spaces, known as *pores* or *voids*, within its structure, usually referred to as the *solid matrix*. The *pore space* is usually filled with one or more fluids (liquid or gas) or a mixture of fluids. The importance of porous media resides in their ability to influence the transport of fluids, such as liquids or gases, through their permeable structure.

A *phase* in a porous medium can be defined as a "chemically homogeneous portion of a system that is separated from other such portions by a definite physical boundary, called interphase boundary" [2, 5]. As gases are completely miscible and can't preserve a physical boundary between them, we must expect the existence of only one gaseous phase in our system, while it is possible to observe more than one liquid phase. If the void space is filled with n fluids, we talk about *n-phase* flow; in particular, in hydrological scenarios, such as the one under consideration, it is common for two phases to be present in the system, which are generally water and air. Delving deeper, a *component* is "part of a phase that is composed of an identifiable homogeneous chemical species, or of an assembly of species" [2, 5]. The quantity of components determines the minimum number of independent substances required to describe the structure of the phase.

The solid matrix and the void space are distributed throughout the porous medium domain. However, their

distribution is not necessarily uniform and the real physical structure of the system is in most cases unknown. The strategy for studying the flow in these complex domains involves treating the porous medium as a continuum, where the properties and relevant quantities are defined pointwise as the averaged quantity inside an arbitrary volume. This volume, often referred to as the *Representative Elementary Volume* (REV), is typically conceptualized as a sphere centered at the physical point. The characteristic length l_{REV} for this sphere must meet the following requirements:

- It must be sufficiently high to contain both solid phase and void space, no matter where we place it within our domain. Pores must be numerous enough to define a mean property and small oscillations in the size of the volume determines small variations in the mean values.
- It must be sufficiently small to approximate the variations of the quantities among different REVs by means of continuous functions.

By exploiting this approach, the equations describing phenomena in porous media involve macroscopic averaged quantities.

Building upon this concept, and with the requirement of a connected pore space, two significant averaged quantities are introduced:

- The porosity $\phi = \phi(\mathbf{x}, t, l_{REV})$ is given by the ratio between the void space and the total volume occupied by the REV centered in $\mathbf{x}$ at time t. It is a property of the porous medium.
- The saturation of phase α, $S_\alpha = S_\alpha, (\mathbf{x}, t, l_{REV})$, is defined as the ratio between the void space occupied by the phase α and the total pore space of the REV centered in $\mathbf{x}$ at time t. It is a property of the phase.

Moreover, the product ϕS_w, where S_w represents the saturation of water, is commonly referred to as the *moisture content*.

2.2. Single-phase flow in a porous medium

In this section, we delve into the governing equations applicable to the single-phase flow context. As mentioned earlier, single-phase flow in a porous medium refers to a scenario where only one fluid phase, typically either liquid or gas, occupies the void spaces within the porous structure.

Towards the conclusion of the section, we present the complete system that describes the fully saturated case under consideration.

The understanding of dynamics in the context of single-phase flow is foundational for approaching the model required for our purposes, namely that of two-phase flow.

2.2.1 Darcy's Law for Single-phase flow

Darcy's law is an equation that models the motion of one fluid inside a fully saturated porous medium. In 1856, Henry Darcy proposed it in the appendix of his book based on empirical findings from experiments involving the flow of water through filter sands [17]. The differential form of the equation is articulated as follows [1]:

$$\mathbf{q} = -\underline{\underline{\kappa}}\boldsymbol{\nabla}\left(\frac{p}{\rho g} + z\right) \tag{1}$$

where $\mathbf{q}$ represents the volumetric flow rate per unit area of the porous medium ($[\mathbf{q}] = LT^{-1}$), $\underline{\underline{\kappa}}$ is the *hydraulic conductivity* ($[\underline{\underline{\kappa}}] = LT^{-1}$), ρ is the fluid density ($[\rho] = ML^{-3}$), p is the pressure of the fluid ($[\overline{p}] = ML^{-1}T^{-2}$), g is the gravity acceleration ($[g] = LT^{-2}$) and z is the quota ($[z] = L$).

Note that the hydraulic conductivity includes both the effects of the solid matrix and the fluid. To separate them, we introduce the concept of *intrinsic permeability* $\underline{\underline{K}}$, which is related only to the skeleton of the porous medium ($[\underline{\underline{K}}] = L^2$). Therefore $\underline{\underline{\kappa}}$ can be expressed as follows:

$$\underline{\underline{\kappa}} = \underline{\underline{K}}\frac{\rho g}{\mu}$$

where μ, which is the liquid viscosity ($[\mu] = ML^{-1}T^{-1}$), is a property of the fluid.

Let ρ now be constant. In this framework, Darcy's law might be rewritten as:

$$\mathbf{q} = -\frac{\underline{\underline{K}}}{\mu}(\boldsymbol{\nabla}p + \rho g\boldsymbol{\nabla}z)$$

Moreover, by introducing two additional quantities, namely the *hydraulic pressure* $\psi = \frac{p}{\rho g}$ $[L]$ and the *hydraulic head* $h = \psi + z$ $[L]$, Darcy's law can be reformulated as follows:

$$\mathbf{q} = -\underline{\underline{\boldsymbol{\kappa}}} \boldsymbol{\nabla} h. \tag{2}$$

We currently have one vector equation, with vector $\mathbf{q}$ and scalar h as the unknowns. This means that additional information is required to solve the problem. The mass conservation equation is derived in the following section.

2.2.2 Mass Conservation Equation for Single-phase flow

In order to deduce the mass balance equation for a single-phase fluid in porous medium, we first consider the balance equation for a domain Ω filled of fluid. Let ρ be the density of the fluid, $\mathbf{v}$ the fluid velocity, $\tilde{f}$ a source of mass of fluid per unit of volume and $V \in \Omega$ an arbitrary fluid volume. It is acknowledged that the mass conservation equation in its differential form is stated as follows:

$$\frac{\partial \rho}{\partial t} + \boldsymbol{\nabla} \cdot (\rho \mathbf{v}) = \tilde{f}. \tag{3}$$

Equation (3) represents the starting point to derive the *mass conservation equation* in the case of porous medium. In the latter case, an auxiliary tool must be introduced to ascertain which phase (fluid or solid) a point $A \in V$ belongs to. The *phase-distribution function* [25] is introduced:

$$\gamma_\alpha(\mathbf{r}, t) = \begin{cases} 1 & \text{if } \mathbf{r} \in V_l \\ 0 & \text{if } \mathbf{r} \in V_s \end{cases}$$

where $\mathbf{r} = \mathbf{x} + \boldsymbol{\xi}$, with $\mathbf{x}$ being the center of the REV and $\boldsymbol{\xi}$ the local coordinate of the point relative to $\mathbf{x}$. Here, V_α represents the region occupied by phase α.

Using the concept of average over the REV on our control volume, as presented by [25], Equation (3) in the case of porous medium can be rewritten as:

$$\int_V \frac{1}{|REV(\mathbf{x}, t)|} \int_{REV(\mathbf{x}, t)} \left(\frac{\partial \rho}{\partial t} - \tilde{f} + \boldsymbol{\nabla} \cdot (\rho \mathbf{v}) \right) \gamma_l(\mathbf{x} + \boldsymbol{\xi}, t) dv_\xi dV = 0. \tag{4}$$

After simplifications and the introduction of average operators, the expression for Equation (4) takes on the following simplified and more practical differential form:

$$\frac{\partial(\phi \rho)}{\partial t} + \boldsymbol{\nabla} \cdot (\phi \rho \mathbf{v}) = f \tag{5}$$

following the computations that can be found in Appendix A. It is important to remember that in (5) we are dealing with averaged quantities.

Let us now suppose that both ρ and ϕ strictly depend on p. By means of the chain rule of differentiation we expand the time derivative at the left-hand side of Equation (5):

$$\frac{\partial(\phi \rho)}{\partial t} = \phi \frac{\partial \rho}{\partial t} + \rho \frac{\partial \phi}{\partial t} = \phi \frac{\partial \rho}{\partial p} \frac{\partial p}{\partial t} + \rho \frac{\partial \phi}{\partial p} \frac{\partial p}{\partial t}.$$

It is a well-known observation from empirical experiments that grains have a tendency to compact when the fluid pressure is decreased [25]. Therefore, we can express the following relations:

$$\frac{\partial \phi}{\partial t} = C_v \frac{\partial p}{\partial t}, \qquad \beta = \frac{1}{\rho} \frac{\partial \rho}{\partial p}$$

where C_v is the *coefficient of consolidation* and β is known as the *compressibility of water*.

By exploiting the latter relations, Equation (5) can be formulated as

$$\rho c_\Sigma \frac{\partial p}{\partial t} + \boldsymbol{\nabla} \cdot (\rho \mathbf{q}) = f \tag{6}$$

where $c_\Sigma = (\phi \beta + C_v)$ and $\mathbf{q} = \phi \mathbf{v}$.

A comparable expression to Equation (6) can be derived by following similar steps, with the hydraulic head as variable instead of the pressure:

$$\rho S_s \frac{\partial h}{\partial t} + \boldsymbol{\nabla} \cdot (\rho \mathbf{q}) = f \tag{7}$$

where $S_s = \rho g c_\Sigma$ is the *specific storage*. Due to the indirect dependence of S_s on h, it introduces a nonlinearity. Nevertheless, it manifests as a weak nonlinearity, enabling us to treat it as approximately constant.

4

Therefore, the final form of the mass conservation equation reads as follows:

$$S_s \frac{\partial h}{\partial t} + \boldsymbol{\nabla} \cdot \mathbf{q} = \frac{f}{\rho} \tag{8}$$

where we simplified the transport term to $\rho \boldsymbol{\nabla} \cdot \mathbf{q}$, being the variation of ρ negligible compared to the divergence of $\mathbf{q}$. Equation (8) presents the expression for groundwater flow commonly encountered in literature. Specifically, in our model, we assume that the snowpack has a constant density, implying incompressibility and resulting in $\beta = 0$. While acknowledging that this is a restrictive hypothesis, considering that snow intrinsically possesses the property of self-compaction, exploring the phenomenon of compressibility remains an interesting avenue for future developments.

2.2.3 Closed system for Single-phase flow

Consider a region, denoted by Ω, which contains a porous medium. Assume that the entire material is completely filled with a single fluid of constant density ρ. Then, the system of equations that govern the motion of the fluid flow in the medium in Ω is:

$$\begin{cases} \mathbf{q} = -\underline{\underline{\boldsymbol{\kappa}}} \boldsymbol{\nabla} h & \text{in } \Omega \times (0, T) \\ S_s \dfrac{\partial h}{\partial t} + \boldsymbol{\nabla} \cdot \mathbf{q} = \dfrac{f}{\rho} & \text{in } \Omega \times (0, T) \end{cases} \tag{9}$$

where, as for the initial condition, it is necessary to impose a condition on h at time t_0.

For what concerns boundary conditions, the preferred setup reads:

- Conditions for the head h on Γ_D,
- Conditions for the normal flux $\mathbf{q} \cdot \mathbf{n}$ on Γ_N,

where $\Gamma_D \cup \Gamma_N = \partial \Omega$ and $\Gamma_D \cap \Gamma_N = \emptyset$.

Note that the presented form is commonly referred to as the *mixed formulation* of the Darcy problem. In a mixed formulation, the condition on h naturally appears in the weak formulation, while the condition on the flux must be manually imposed, categorizing it as an essential condition.

2.3. Two-phase flow in a porous medium

This thesis focuses on a physical problem that revolves around the concept of two-phase flow in a porous medium, that is, when two or more phases occupy the pore space. In particular, the system in our scenario encompasses two phases: water and air.
The theory initially formulated for single-phase flow is restructured to model the interaction between the two phases and the rock matrix. The mass conservation equation for every phase α is derived in Section 2.3.1, while in Section 2.3.2 we introduce the two-phase Darcy's law. Subsequently, in Section 2.3.3 we investigate the important relationship between two important quantities, capillary pressure and saturation, leading us to unveil the comprehensive two-phase fluid system in Section 2.3.4. Finally, in Section 2.4, the problem is contextualized to the case of a porous medium partially saturated by water, with the remaining fraction of the void space filled by air. In this scenario, the system is simplified through the introduction of the Richards' equation.

2.3.1 Mass conservation Equation for Two-phase flow

When working with two fluids, it becomes necessary to assign distinct roles to each of them; in particular, there is often an observable difference in the affinity of one fluid for the solid surface compared to the other. Known as the *wetting fluid*, this fluid exhibits a greater tendency to wet the solid surface. Conversely, the second fluid is referred to as the *non-wetting fluid*. The conventional metric for assessing wettability is provided by the contact angle, which is defined as the angle formed between the solid surface and the interface separating the two fluids: specifically, the *wetting fluid* is identified as the one occupying the region within the acute angular space. In our scenario, water is categorized as the wetting fluid and air is the nonwetting fluid.

By replicating the procedures outlined in Section 2.2.2, assuming the immiscibility of the two phases, we can establish individual mass conservation equations for each phase α [25]:

$$\frac{\partial}{\partial t}(\rho_\alpha \phi S_\alpha) + \boldsymbol{\nabla} \cdot (\rho_\alpha \mathbf{q}_\alpha) = f_\alpha \tag{10}$$

where, in general, when handling the wetting or non-wetting fluid, $\alpha = w$, nw respectively. In Equation (10) ρ_α, S_α, $\mathbf{q}_\alpha$ and f_α represent respectively the density, the saturation, the specific storage and the source/sink term of phase α.

It's crucial to emphasize that in the scenario of a fully saturated system, where only one fluid occupies the pore space, the saturation term S_α becomes equal to 1. Consequently, Equation (10) simplifies to the conventional mass balance equation for a single-fluid system described in Section 2.2.2.

For each phase α, both S_α and $\mathbf{q}_\alpha$ are the unknowns.

2.3.2   Darcy's law for Two-phase flow

The difficulty in formulating Darcy's law for two-fluid flow arises from the need to consider the effects resulting from the presence of more than one fluid within the pore space. In a two-phase fluid framework, the space available for every phase α to flow is reduced, as two fluids reside in the pore space. Therefore we expect the permeability of phase α to diminish as its own saturation decreases. To model this interaction, the concept of *relative permeability* $k_{r\alpha}(S_\alpha)$ for the phase α is introduced:

$$k_{r\alpha}(S_\alpha) = \frac{q_\alpha(S_\alpha)}{q_\alpha^{sat}}$$

where $q_\alpha(S_\alpha)$ and q_α^{sat} represent fluxes in two different circumstances: while the first one characterizes the partially saturated case, in the second one the pore space is completely saturated with fluid phase α. By construction, it is a dimensionless quantity and it's a nonlinear function of saturation. Furthermore, the saturation of the wetting fluid S_w^{res} such that $k_{rw}(S_w^{res}) = 0$ is not usually zero. This situation arises when some fluid still occupies some pore space, but there are no spatial connections that enable flow. This nonflowing saturation is commonly known as the *residual saturation* [4]. In Section 3.3, we present specific shapes and analytical expressions for $k_{r\alpha}$ customized for our model.

Finally, it is important to take into account that each fluid possesses its unique pressure. Therefore, Darcy's equation for a two-fluid system may be written as follows [25]:

$$\mathbf{q}_\alpha = -\frac{\underline{\underline{\boldsymbol{K}}} k_{r\alpha}}{\mu_\alpha}(\boldsymbol{\nabla} p_\alpha - \rho_\alpha g \boldsymbol{\nabla} z) \tag{11}$$

where p_α represents the specific pressure of fluid α.

2.3.3   Pressure-Saturation Constitutive Relations

Assuming prior knowledge of porosity, fluid densities and source/sink terms, Equations (10) and (11), which, in three dimensions, correspond to four scalar equations, introduce five unknown scalar quantities for each phase α. These include fluid pressure, fluid saturation, and the three components of the fluid volumetric flux.

Thus, in a system involving two fluids, there are ten variables that need to be determined, but only eight equations are at hand. To adequately close the system, supplementary equations are necessary.

A simple correlation can be established through a basic volume consideration, ensuring that the entire pore space is filled by fluid with no coexistence or overlap of phases. This restriction can be formulated as follows:

$$\sum_\alpha S_\alpha = 1. \tag{12}$$

which serves as ninth equation.

The final equation is established through a functional connection between S_α and the *capillary pressure* P_c, defined as the pressure disparity between the nonwetting and wetting fluid. To comprehend the underlying physical basis of this connection, it is essential to examine the multifluid system at the pore scale. At this scale, fluid phases are separated by distinct fluid-fluid interfaces, which arise due to minute attractive forces within the fluid phases. These forces give rise to interfaces exhibiting a mechanical characteristic, akin to a thin flexible membrane, which can withstand a certain level of stress without breaking. Stress across a fluid-fluid interface occurs when the pressures on either side of the interface are unequal and it manifests through the curvature exhibited by the interface [25].

Increasing, for example, nonwetting fluid pressure, while keeping wetting fluid pressure constant, leads to instability along the boundary, causing drainage. The interface travels through the porous medium, potentially splitting, until it reaches a new stability in smaller pores under the applied pressure difference [25]. Once achieved a new equilibrium, by measuring pressures and wetting fluid outflow for each state, the functional relationship between fluid saturation and capillary pressure can be derived. A specific shape and a model for this relationship are detailed in Section 3.3, where the correlation is expressed in terms of ψ and $\theta = \phi S$.

6

2.3.4 Closed system for Two-phase flow

Consider a domain Ω, encompassing a porous medium filled entirely with two fluids. The system of equations governing the two-phase flow within the medium in Ω reads as follows:

$$
\begin{cases}
\dfrac{\partial}{\partial t}(\rho_w \phi S_w) + \boldsymbol{\nabla} \cdot (\rho_w \mathbf{q}_w) = f_w & \text{in } \Omega \times (0,T) \\[2mm]
\dfrac{\partial}{\partial t}(\rho_{nw} \phi S_{nw}) + \boldsymbol{\nabla} \cdot (\rho_{nw} \mathbf{q}_{nw}) = f_{nw} & \text{in } \Omega \times (0,T) \\[2mm]
\mathbf{q}_w = -\underline{\boldsymbol{\kappa}} k_{rw}(\boldsymbol{\nabla} h_w) & \text{in } \Omega \times (0,T) \\[2mm]
\mathbf{q}_{nw} = -\underline{\boldsymbol{\kappa}} k_{rnw}(\boldsymbol{\nabla} h_{nw}) & \text{in } \Omega \times (0,T) \\[2mm]
S_w + S_{nw} = 1 & \text{in } \Omega \times (0,T) \\[2mm]
F_w(P_c, S_w) = 0 & \text{in } \Omega \times (0,T)
\end{cases}
\tag{13}
$$

where, in our case, w may represent water, while $nw = a$ might represent air. In particular, $F_w(P_c, S_w)$ represents the model that links the capillary pressure to the water saturation.

2.4. A simplification: the Richards' equation

In the hydrogeological context, the unsaturated zone represents an area of prominent importance. This zone is a two-phase porous media system, where, as previously stated, water acts as the wetting fluid, and air acts as the nonwetting fluid. This situation is typical of shallow layers of the subsurface, and occurs also in the case of snow permeated by rain or water originating from melting. Simplifications of the two-fluid system within this domain are feasible due to the specific physical properties of the involved fluids.

Considering atmospheric conditions, specifically at $1\,\text{atm}$ and $20\,^\circ\text{C}$, air exhibits a density of approximately $1\,\text{kg/m}^3$ and a viscosity of around $1.8 \times 10^{-5}\,\text{Pa} \cdot \text{s}$. In contrast, at the same conditions, water has a density of approximately $1000\,\text{kg/m}^3$ and a viscosity of roughly $10^{-3}\,\text{Pa} \cdot \text{s}$. Therefore, air is significantly less dense and less viscous than water, leading to much smaller pressure gradients in unsaturated soils. The two-fluid version of Darcy's equation suggests that, to achieve a certain volumetric flux, the pressure gradient required for air is about 100 times less than that needed for water. Consequently, the air pressure in the unsaturated zone remains comparable to atmospheric pressure due to its low density and viscosity, allowing for some simplifications in the overall two-fluid system. This concept is known as *Richards' assumption*, named after L. A. Richards who introduced soil water flow equations in 1931 [28]. Richards' assumption doesn't mean the air phase is static, but it is based on the idea that the air phase has extremely low viscosity, making it practically inviscid. In such a case, the air phase is highly mobile and can move without notable pressure gradients.

By adopting this assumption, we can exclude air pressure from the set of unknowns of our system. Additionally, through the combination of Darcy's equation with the water mass balance equation and the elimination of S_a using the algebraic constraint on saturations, we simplify our system to two equations: the water mass balance equation and the $P_c - S$ relationship. The two remaining unknowns are therefore S_w and p_w.

Assuming $p_a = p_{\text{atm}} = 0$, we obtain $P_c = -p_w$. Consequently, the $P_c - S$ relationship implies a $p_w - S$ correlation, allowing all equations to be expressed in terms of these two variables.

With these considerations, the revised formulation of System (13) is presented as follows:

$$
\begin{cases}
\dfrac{\partial}{\partial t}(\rho_w \theta_w) - \boldsymbol{\nabla} \cdot \left(\rho_w \dfrac{\underline{\underline{\boldsymbol{K}}} k_{rw}}{\mu_w}(\boldsymbol{\nabla} p_w + \rho_w g \boldsymbol{\nabla} z) \right) = f_w & \text{in } \Omega \times (0,T) & \text{(14a)} \\[3mm]
g_w(p_w, S_w) = 0 & \text{in } \Omega \times (0,T) & \text{(14b)}
\end{cases}
$$

where $\theta_w = \phi S_w$.

Usually, instead of p_w, the variable $\psi_w = \dfrac{p_w}{\rho_w g}$ is employed. Assuming ρ_w to be constant, System (14) can be rewritten as:

$$
\begin{cases}
\dfrac{\partial \theta_w}{\partial t} - \boldsymbol{\nabla} \cdot [\underline{\underline{\boldsymbol{\kappa}}}_{sat}^w k_{rw}(\boldsymbol{\nabla} \psi_w + \boldsymbol{\nabla} z)] = \dfrac{f_w}{\rho_w} & \text{in } \Omega \times (0,T) \\[3mm]
\omega_w(\psi_w, S_w) = 0 & \text{in } \Omega \times (0,T)
\end{cases}
\tag{15}
$$

where $\underline{\underline{\boldsymbol{\kappa}}}_{sat}^w = \underline{\underline{\boldsymbol{\kappa}}}$ of the fully saturated case and $\omega_w(\psi_w, S_w)$ is the relationship that links ψ_w with S_w.

Regarding the initial condition, usually condition on ψ_w at time t_0 should be imposed.

For what concerns boundary conditions, the preferred setup reads:
- Dirichlet conditions for the pressure head ψ_w on Γ_D
- Neumann conditions for the flux $\mathbf{q}_w \cdot \mathbf{n} := \underline{\underline{\boldsymbol{\kappa}}}^w_{sat} k_{rw} (\boldsymbol{\nabla}\psi_w + \boldsymbol{\nabla}z) \cdot \mathbf{n}$ on Γ_N

where $\Gamma_D \cup \Gamma_N = \partial\Omega$ and $\Gamma_D \cap \Gamma_N = \emptyset$.

Finally, note that:

- For $\psi \leq 0$, we find ourselves in the unsaturated zone, where the saturation of each phase is less than one.
- For $\psi > 0$ the fluid content is equal to the porosity and we are in the fully saturated case. When saturation attains value 1, the function $\theta(\psi)$ is not invertible anymore and due to its derivative approaching zero we have that Richards' equation degenerates from parabolic to elliptic. This implies that under these conditions saturation can't be considered as a primary variable [4].
- For values of $\psi > 0$, the conductivity in the Richards' case equals the permeability in the Darcy case.
- When saturation tends to zero, that is, for significantly negative values for ψ, the relative conductivity tends to vanish. This implies that the medium becomes nearly impermeable under such conditions. In this scenario we may encounter some problems from the numerical point of view, especially with methods such as the Newton Method. The method exhibits quadratic convergence when the initial guess is sufficiently close to the exact solution. However, issues arise with the linear system, as the jacobian matrix on the left-hand side involves $k'(\theta(\psi))$ and $\theta'(\psi)$, which may diverge to extremely high values. This ill-conditioned problem may prevent the Newton Method from converging [4].

3. Infiltration and Refreezing of Melt in Snow

The movement of surface-generated meltwater into a snowpack represents a significant yet poorly understood process. Developing a reliable model for meltwater flow through snow is essential for accurate predictions in broader-scale models of snow cryohydrology and glaciology [23]. Although the generation of melt at the snow surface tends to be relatively uniform across space, the infiltration of meltwater through an underlying snowpack, physically speaking, is highly heterogeneous due to gravity fingering instabilities. This diversification leads to the formation of vertical preferential flow pathways and lateral flow pathways guided by areas of low permeability, such as ice pipes.
Both types of preferential pathways have been observed in the field through different studies such as those described in [8, 12]. Specifically, experiments conducted in laboratory settings have demonstrated that the percolation of meltwater into snowpacks is inherently unstable, akin to gravity-driven water infiltration through dry soil [18]. Moreover, when melt interacts with a snowpack, it has the tendency to rapidly refreeze, forming ice and diminishing the local snow porosity. This refreezing mechanism not only reduces the effective infiltration rate by utilizing available liquid water for transport but also lowers the hydraulic conductivity of snow.

Traditionally, the infiltration of meltwater through a snowpack is modeled using the Richards' equation. However, this equation faces limitations in accurately reproducing unstable infiltration patterns. As suggested by [23], an extension to Richards' equation by means of a fourth-order term in saturation allows to capture the empirically observed instabilities.
Nonetheless, in this study, our primary focus is not on capturing instabilities but on understanding how infiltration mechanics, together with the thermodynamic aspect, define the overall process of melt transport. Consequently, in this research, we adopt the classical Richards' equation, mindful that including the mentioned extra term would introduce additional nonlinearities, thereby increasing the complexity of an already intricate problem. Without the additional term, whose inclusion could significantly enrich the depth of analysis in future investigations, we anticipate observing stable infiltration fronts rather than unstable preferential infiltration.

Finally, in thermodynamic terms, the model incorporates a non-isothermal condition, specifically considering the influence of latent heat release during phase change and its impact on the thermal energy balance of the snowpack. This thesis uses a dual-temperature field framework, namely adopting a LTNE condition. The governing equations for these temperature fields are discussed in Section 3.4.

3.1. Introduction to the mathematical model

Fluid infiltration into dry soil is a well-explored subject in literature. When water and air are the phases of the system, the use of Richards' equation is common, and the challenging resolution of this equation, hindered by its nonlinearities, is extensively studied in its overall behavior. The challenge in modeling the infiltration of water into a snowpack lies in the fact that the infiltrating phase, water, shares identical chemical properties with the medium it infiltrates in, which is ice. The only differentiating factor between them is their physical

state.

As a result, the modeling process must take into account not only the mechanics of infiltration due to gravity effects but also the thermodynamics that governs phase changes.

We introduce a model that combines the behavior of water infiltration in unsaturated porous media with the non-equilibrium thermodynamics controlling ice-water phase transitions.

As previously mentioned, the snowpack is considered as a porous medium comprising water, air, and ice, where water functions as the wetting fluid, air as the nonwetting fluid, and ice as the solid matrix. The unknowns of the model are defined as volume-averaged quantities over a REV and are:

- Porosity $\phi(\mathbf{x}, t)$,
- Water Saturation $S(\mathbf{x}, t)$,
- Hydraulic pressure of water phase $\psi(\mathbf{x}, t)$,
- Darcy velocity of melt infiltration $\mathbf{q}(\mathbf{x}, t)$,
- Ice temperature $T_i(\mathbf{x}, t)$,
- Water temperature $T_w(\mathbf{x}, t)$,

where, in line with Richards' assumption, the unknowns associated with air have been excluded from the model. The mass conservation equations for ice and water are described in Section 3.2, while Section 3.3 defines the dynamics of unsaturated meltwater flow. Finally, arguments related to thermodynamics are addressed in Section 3.4.

3.2. Mass Conservation

The ice mass conservation equation can be written as

$$\rho_i \frac{\partial(1-\phi)}{\partial t} = -\rho_i R_m W_{SSA}(T_{int} - T_{melt}), \tag{16}$$

where ρ_i is the density of ice, which is assumed to be constant, R_m is the rate coefficient of the phase change, $W_{SSA} = W_{SSA}(S, \phi)$ is referred to as the *wet specific area*, $T_{int} = T_{int}(T_i, T_w)$ is an averaged temperature for the ice-water interface and T_{melt} is the melting temperature. Further specifications about the thermal quantities can be found in Section 3.4. The right-hand side in Equation (16) stands for the quantity of ice mass which is lost or gained due to melting or refreezing, respectively.

The constant coefficient R_m ($[R_m] = LK^{-1}T^{-1}$) has the following expression:

$$R_m = \frac{c_w}{\beta_{sol} L_{sol}}$$

where c_w is the *water specific heat capacity* ($[c_w] = L^2 T^{-2} K^{-1}$), β_{sol} is the kinetic attachment index ($[\beta_{sol}] = TL^{-1}$) and L_{sol} denotes the solidification latent heat ($[L_{sol}] = L^2 T^{-2}$).

The function $W_{SSA}(S, \phi)$ represents the area per unit volume of the interface between ice and water and can be modeled as a function of saturation and porosity [20] as

$$W_{SSA}(S, \phi) = (S - S_l) \frac{SSA_0}{\phi_0 ln(\phi_0)} \phi ln(\phi),$$

where SSA_0 is the initial *snow specific area of the snowpack* ($[SSA_0] = L^{-1}$) and $S_l = 10^{-3}$ is a regularizing term.

Regarding the wetting fluid, the water mass conservation equation can be written as

$$\rho_w \left(\frac{\partial \theta(\psi)}{\partial t} + \boldsymbol{\nabla} \cdot \mathbf{q} \right) = \rho_i R_m W_{SSA}(T_{int} - T_{melt}) \tag{17}$$

where ρ_w is the water density, which is assumed to be constant, $\mathbf{q}$ is the Darcy velocity ($[\mathbf{q}] = LT^{-1}$), and $\theta(\psi) = \phi S(\psi)$ ($[\theta(\psi)] = 1$).

Note that the right-hand side of Equation (17) addresses the gain or loss of liquid mass. In order to guarantee mass conservation during the phase change process, the right-hand side terms in Equation (16) and Equation (17) have opposite signs but the same magnitude.

3.3. Unsaturated Meltwater Flow

As mentioned earlier, this work employs the classical expression for the Richards equation.

The meltwater Richards' flux reads

$$\mathbf{q} = -K_s(\phi)k_r(\psi)\boldsymbol{\nabla}\Pi(\psi) \tag{18}$$

where $k_r(\psi)$ is the water relative hydraulic conductivity, $K_s(\phi)$ is the snow hydraulic conductivity in the fully saturated case and $\Pi(\psi) = \psi + z$ is the overall flow potential.

Before detailing the expressions for $K_s(\phi)$ and $k_{rw}(\psi)$, it is crucial to establish the relationship between the water hydraulic pressure ψ and the moisture content θ. In this context, we employ the Van Genuchten model [32] with appropriate parameter calibration:

$$\theta(\psi) = \begin{cases} \theta_r + \dfrac{\theta_s - \theta_r}{[1 + (-\alpha\psi)^n]^{\frac{n-1}{n}}} & \text{if } \psi \leq 0 \\ \theta_s & \text{if } \psi > 0 \end{cases} \tag{19}$$

where $\theta_s = S_{w,sat}\phi = \phi$ is the water content in the fully saturated case and $\theta_r = S_w^{res}\phi$ is the residual water content. Note that, for clarity in notation, we are omitting the subscript w.

Regarding the parameters α and n, they depend on the material forming the solid skeleton, in particular on the ratio between the dry bulk density of snow $\rho_{snow} = \rho_i(1 - \phi)$ and its grain size diameter d_i ($[d_i] = L$). We assume ρ_{snow} and d_i to be constant during the physical process, due to the lack of information about their evolution as the microstructure of the snow changes. To establish the relationship between ρ_{snow}/d_i and the Van Genuchten parameters α and n, we rely on the fitting outcomes presented by Yamaguchi et al. [34], which are depicted in Figure 1:
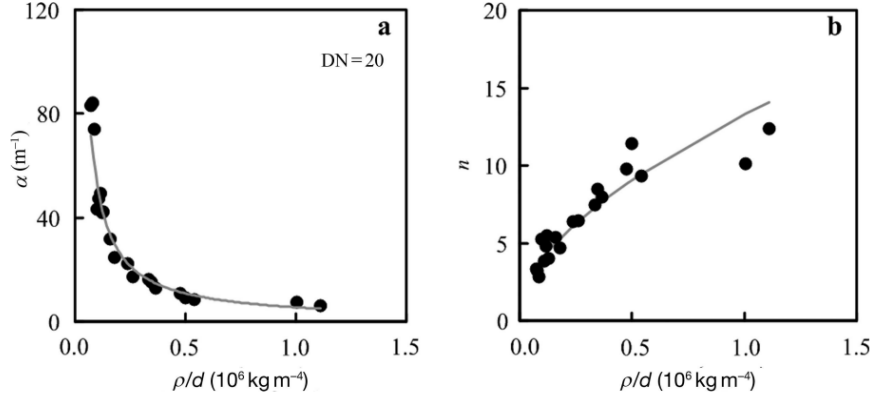

Figure 1: Dependence of α (left) and n (right) on the ratio ρ_{snow}/d_i. The data points are determined by empirical results, while the curves are defined by the fitted model (from [34]).

The fitted model has the following analytical expression:

$$\alpha = 4.4 \times 10^6 \left(\frac{\rho_{\text{snow}}}{d_i}\right)^{-0.98}$$
$$n = 1 + 2.7 \times 10^{-3} \left(\frac{\rho_{\text{snow}}}{d_i}\right)^{0.61} \tag{20}$$

where d_i is expressed in meters. The model aligns well with experimental data, exhibiting high correlation values ($R = 0.98$ for α, $R = 0.93$ for n).

Concerning the expression for the absolute conductivity $K_s(\phi)$, we adopt the empirical expression proposed in [7] ($[K_s] = LT^{-1}$):

$$K_s(\phi) = 3\left(\frac{d_i}{2}\right)^2 \frac{\rho_w g}{\mu_w} exp[-0.013\rho_{snow}(\phi)] \tag{21}$$

while, for the relative hydraulic conductivity, the Van Genuchten-Mualem model [24] is employed:

$$k_r(\psi) = \Theta(\psi)^{\frac{1}{2}}\left[1 - \left(1 - \Theta(\psi)^{\frac{1}{m}}\right)^m\right]^2 \tag{22}$$

where $m = 1 - \dfrac{1}{n}$ and $\Theta = \dfrac{\theta - \theta_r}{\theta_s - \theta_r}$ is the effective saturation.
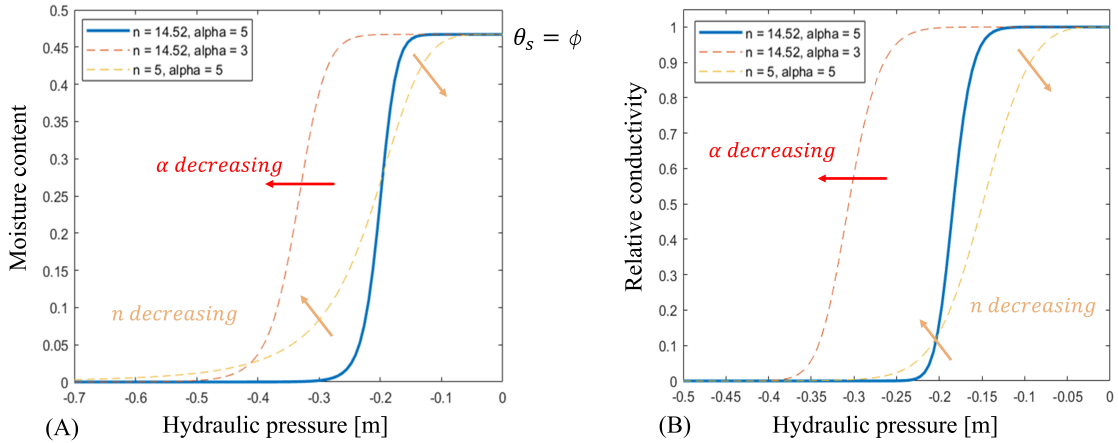
Figure 2: The maximum derivative of θ (A) and k_r (B) increases with higher values of α and n.

In Figure 2 we present the shapes for $\theta(\psi)$ and $k_r(\psi)$ for different values of n and α. It is clear that the profiles of $\theta(\psi)$ and $k_r(\psi)$ become steeper with increasing values of α and, most notably, n. Be aware that the values of α and n within the range depicted in this plot, which coincide with those we will consider for our model, are categorized as "extreme values". In general, in porous media such as soil, these parameters are conventionally characterized by values around $\alpha_{\text{soil}} \approx 0.5$ and $n_{\text{soil}} \approx 2$, as reported in [14], with $\max_\psi |\theta'(\psi)| \approx 10^{-2}$. For the case of snow, instead, we obtain $\max_\psi |\theta'(\psi)| \approx 10^0$. This will be a compelling subject in Section 4.3.2 when discussing convergence of the nonlinear solver.

Given a specified rectangular region of the two-dimensional space denoted as Ω, the boundary conditions pertaining to Richards' equation for this model are the following:

$$\begin{aligned} \mathbf{q} \cdot \mathbf{n} &= 0 && \text{on } \Gamma_l \cup \Gamma_b \\ \psi &= \psi_{top} > 0 && \text{on } \Gamma_t \end{aligned} \tag{23}$$

where Γ_t represents the upper boundary portion, Γ_b identifies the lower part of the boundary, and Γ_l designates the lateral boundary section, with $\Gamma_t \cup \Gamma_b \cup \Gamma_l = \partial\Omega$ and $\Gamma_i \cap \Gamma_j = \emptyset \ \forall i \neq j$. While the first condition prescribes zero mass flux through the lateral and bottom boundaries, the second condition enforces a constant pressure at the top with the goal of simulating a source of full saturation. This condition represents a perpetual source of water intended to infiltrate into the snowpack.

3.4. Thermal Balance

In addition to addressing the phase change process of melt refreezing in Equation (16), as detailed in Section 3.2, we also consider phase change by adjusting the thermal budget, accounting for the exchange of heat between the ice and water phases. Our model incorporates the assumption of LTNE, permitting the simultaneous existence of ice and water phases at different temperatures and allowing us to estimate the rate of ice-water phase change as a function of both ice and water temperatures.

The temperature evolution equations for ice and water phases read as follows:

$$\rho_i c_i \frac{\partial [(1-\phi)T_i]}{\partial t} = \boldsymbol{\nabla} \cdot (K_i (1-\phi)\boldsymbol{\nabla} T_i) - \alpha_i \rho L_{sol} R_m W_{SSA}(T_{int} - T_{melt}), \tag{24}$$

$$\rho_w c_w \left[\frac{\partial(\phi S T_w)}{\partial t} + \boldsymbol{\nabla} \cdot (\mathbf{q} T_w) \right] = \boldsymbol{\nabla} \cdot (K_w \phi S \boldsymbol{\nabla} T_w) - \alpha_w \rho L_{sol} R_m W_{SSA}(T_{int} - T_{melt}) \tag{25}$$

where c_α and K_α denote the specific heat capacity and thermal conductivity of phase α, respectively. Note that the thermal energy equation for water encompasses both a diffusive and convective term, whereas the ice temperature equation exhibits solely diffusive behavior.

In theory, the choice for the value of ρ on the right-hand side of both equations depends on the direction of the phase change; precisely, $\rho = \rho_i$ for melting and $\rho = \rho_w$ for freezing. However, in practice, it is common to set $\rho = \rho_w$.

Let us now focus on the interface temperature T_{int}, which has been already introduced in Section 3.2. The generalized Stefan solidification model [15] is employed to determine the temperature at the interface between ice and water. With respect to the aforementioned method, at the microscopic level we take into account the following conditions on the moving interface between ice and water Γ_{iw}:

$$T_{int}^P = T_i^P|_{\Gamma_{iw}} = T_w^P|_{\Gamma_{iw}} \qquad \text{(continuity of temperatures)} \qquad (26)$$

$$K_i \boldsymbol{\nabla} T_i^P|_{\Gamma_{iw}} \cdot \mathbf{n}_i - K_w \boldsymbol{\nabla} T_w^P|_{\Gamma_{iw}} \cdot \mathbf{n}_i = L_{sol} \rho_w v_n \qquad \text{(thermal energy conservation)} \qquad (27)$$

$$\frac{T_{int}^P - T_{melt}}{L_{sol}/c_w} = -d_0 \chi - \beta_{sol} v_n \qquad \text{(Gibbs-Thomson condition)} \qquad (28)$$

where the superscript P identifies quantities defined at pore-scale, $\mathbf{n}_i$ is the outward unit normal to the ice-water interface pointing towards water phase, χ is the curvature of Γ_{iw}, v_n is the velocity of the moving interface and T_{int}^P is the temperature at the interface.

By averaging Equations (27) and (28) over Γ_{iw} in a REV, and assuming the interface to have null average curvature ($\overline{\chi} = 0$), we obtain the following Darcy-scale relations:

$$K_i \overline{\boldsymbol{\nabla} T_i^P}|_{\Gamma_{iw}} - K_w \overline{\boldsymbol{\nabla} T_w^P}|_{\Gamma_{iw}} = L_{sol} \rho \overline{v}_n \qquad (29)$$

$$\frac{\overline{T_{int}^P} - T_{melt}}{L_{sol}/c_w} = -\beta_{sol} \overline{v}_n \qquad (30)$$

where $\overline{\eta} = \dfrac{\int_{\Gamma_{iw}} \eta \cdot \mathbf{n}_i da}{\int_{\Gamma_{iw}} da}$ is the Darcy-scale version of η.

Subsequently, to derive a practical algebraic representation for T_{int}, we make the following assumption about the linear relationship between pore-scale temperature gradients and Darcy-scale temperatures T_i and T_w (see Figure 3):

$$\overline{\boldsymbol{\nabla} T_i^P}|_{\Gamma_{iw}} = \frac{T_{int} - T_i}{r_i}, \qquad \overline{\boldsymbol{\nabla} T_w^P}|_{\Gamma_{iw}} = \frac{T_w - T_{int}}{r_w} \qquad (31)$$

where the estimation of r_α, $\alpha = i, w$, is conducted through pore-scale simulations solving a phase-field model for water solidification [15], with the expressions $r_i = 0.06 d_i$ and $r_w = 1.35 r_i$ as a result.
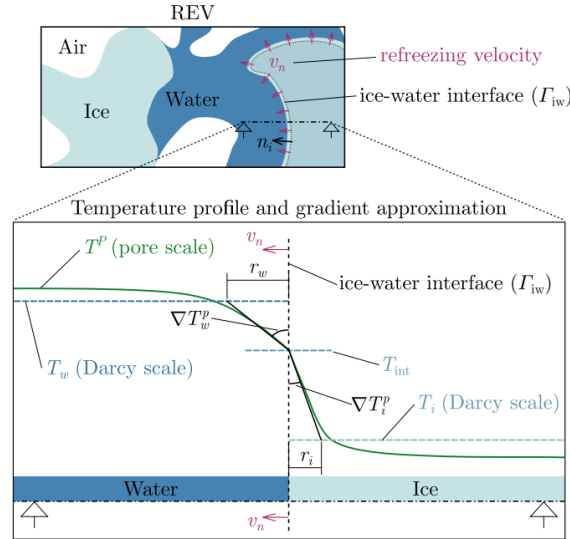

Figure 3: Approximation of the pore-scale temperature gradients on the ice-water interface Γ_{iw} (from [23]).

Combining Equations (29), (30), (31) we can express T_{int} as a function of T_i and T_w:

$$T_{int}(T_i, T_w) = \frac{\dfrac{c_w}{L_{sol}} T_{melt} + \dfrac{\beta_{sol} K_i}{\rho L_{sol} r_i} T_i + \dfrac{\beta_{sol} K_w}{\rho L_{sol} r_w} T_w}{\dfrac{c_w}{L_{sol}} + \dfrac{\beta_{sol} K_i}{\rho L_{sol} r_i} + \dfrac{\beta_{sol} K_w}{\rho L_{sol} r_w}} \qquad (32)$$

where we assumed $\overline{T_{int}^P} = T_{int}$.

Finally, we still need to investigate the characteristics of the α_i and α_w coefficients in Equations (24), (25). They are formulated as follows [23]:

Parameter	Description	Value	Units
ρ_i	Ice density	919	kg m^{-3}
ρ_w	Water density	1000	kg m^{-3}
ρ_{snow}	Snow density	489	kg m^{-3}
c_i	Ice specific heat capacity	1.96×10^{-3}	J kg^{-1} $^\circ$C^{-1}
c_w	Water specific heat capacity	4.2×10^{-3}	J kg^{-1} $^\circ$C^{-1}
L_{sol}	Solidification latent heat	3.34×10^5	J kg^{-1}
β_{sol}	Kinetic attachment coefficient	800	s m^{-1}
K_i	Ice thermal conductivity	2.29	W m^{-1} $^\circ$C^{-1}
K_w	Water thermal conductivity	0.554	W m^{-1} $^\circ$C^{-1}
T_{melt}	Freezing temperature	0	$^\circ$C
g	Gravitational acceleration	9.81	m s^{-2}
μ_w	Water dynamic viscosity	1.792×10^{-3}	kg m^{-1} s^{-1}
SSA_0	Snow surface area	3514	m^{-1}
S_l	Minimum Saturation	1×10^{-3}	1
d_i	Grain size	0.423×10^{-3}	m

Table 1: Physical parameters of the model.

$$\alpha_i = \frac{K_i \dfrac{T_{int} - T_i}{r_i}}{K_i \dfrac{T_{int} - T_i}{r_i} + K_w \dfrac{T_{int} - T_w}{r_w}}, \qquad \alpha_w = \frac{K_w \dfrac{T_{int} - T_w}{r_w}}{K_i \dfrac{T_{int} - T_i}{r_i} + K_w \dfrac{T_{int} - T_w}{r_w}} \tag{33}$$

and they quantify the heat exchange between ice and water averaged over the volume, whether there is a phase change or not. In particular, α_α represents the thermal energy released/absorbed by phase α. Air is excluded from the heat transfer system due to its low specific heat capacity.

In a rectangular 2D domain Ω, the boundary conditions for Equations (24), (25) are the following:

$$
\begin{aligned}
D_i(1-\phi)\boldsymbol{\nabla}T_i \cdot \mathbf{n} = 0, \quad & (D_w \phi S \boldsymbol{\nabla}T_w - \mathbf{q}T_w) \cdot \mathbf{n} = 0 \quad && \text{on } \Gamma_l \\
T_i = T_{melt}, \quad & T_w = T_{melt} \quad && \text{on } \Gamma_t \\
T_i = T_{i,b}, \quad & (D_w \phi S \boldsymbol{\nabla}T_w - \mathbf{q}T_w) \cdot \mathbf{n} = 0 \quad && \text{on } \Gamma_b
\end{aligned}
$$

where Γ_t represents the upper boundary portion, Γ_b identifies the lower part of the boundary, and Γ_l designates the lateral boundary section, with $\Gamma_t \cup \Gamma_b \cup \Gamma_l = \partial\Omega$ and $\Gamma_i \cap \Gamma_j = \emptyset \, \forall i \neq j$. While the Neumann conditions specify zero flux at the respective boundaries, the Dirichlet conditions enforce distinct values for T_i and T_w.

3.5. Physical Parameters

The physical parameters of the problem are collected in Table 1.
Concretely, the parameter d_i is designated as the average diameter of the grain size. In this study, we exclusively examine a specific type of snow characterized by relatively small grains, as detailed in [18], with the average diameter d_i reported in Table 1.
With this choice for d_i and exploiting the expressions presented in (20), the resulting values for the Van Genuchten parameters are $n = 14.52$ and $\alpha = 5$, corresponding to the blue curves in Figure 2. The significant steepness characterizing the curves of $\theta(\psi)$ and $k_r(\psi)$ constitutes a crucial feature for the subsequent analysis of the model and its numerical convergence.
Finally, the value $S_w^{rel} = 0.001$ is chosen as residual saturation, so that we obtain $\theta_r = 0.001\phi$.

4. Computational Framework

In this section, we delineate the numerical strategy for discretizing the equations that constitute the model. Section 4.1 introduces the discretization method applied to Richards' equation, specifically utilizing the Backward Euler scheme for time discretization and the Mixed Finite Element method for spatial discretization. Subsequently, in Section 4.2, we detail the discretization approach for the thermodynamics-related equations, employing once again the Backward Euler method for temporal discretization and the Finite Volumes method

for spatial discretization. Ultimately, we outline the generic numerical setup and coupling strategy that have been employed.

4.1. Discretization of Richards' equation in mixed form

To solve Richards' equation numerically, the following systematic approach is adopted. First, we derive its weak formulation in Section 4.1.1, followed by the temporal discretization of the weak forms in Section 4.1.2. Consequently, to obtain an approximate solution to the time-discretized problem, we employ the Galerkin method in Section 4.1.3. Finally, the equations are spatially discretized using the Mixed Finite Element method, as discussed in Section 4.1.5.

4.1.1 Weak Formulation for the Richards' equation

To derive the weak formulation for the Richards' system given by (17), (18) we begin by introducing two appropriate spaces for the test functions. Let $H_{\nabla\cdot}(\Omega)$ be the space of $L^2(\Omega)$ functions whose divergence belongs to $L^2(\Omega)$ in a weak sense, analytically $H_{\nabla\cdot}(\Omega) = \{\mathbf{v} \in [L^2(\Omega)]^n : \nabla \cdot \mathbf{v} \in L^2(\Omega)\}$. We introduce the following spaces:

$$\mathbf{V} = \{\mathbf{v} \in H_{\nabla\cdot}(\Omega) : \mathrm{tr}_{\boldsymbol{\nu}}\mathbf{v} = r \text{ on } \Gamma_N\},$$
$$\mathbf{V}_0 = \{\mathbf{v} \in H_{\nabla\cdot}(\Omega) : \mathrm{tr}_{\boldsymbol{\nu}}\mathbf{v} = 0 \text{ on } \Gamma_N\},$$
$$Q = L^2(\Omega),$$

where $\mathrm{tr}_{\boldsymbol{\nu}} : H_{\nabla\cdot}(\Omega) \longrightarrow H^{-\frac{1}{2}}(\partial\Omega)$ is the normal trace operator associated with the unit normal vector $\boldsymbol{\nu}$. Clearly, we have $\mathbf{V}_0 \subset \mathbf{V}$.

In addition, we assume the following:

- $\hat{f} = \dfrac{f}{\rho_w} = \dfrac{\rho_i}{\rho_w} R_m W_{SSA}(T_{int} - T_{melt}) \in L^2(\Omega)$,
- The initial conditions $\mathbf{q}_0 \in \mathbf{V}$ and $\psi_0 \in Q$ are known,
- We enforce Dirichlet conditions $\psi = s \in H^{\frac{1}{2}}(\Gamma_D)$ on Γ_D,
- We enforce Neumann conditions $\mathbf{q} \cdot \boldsymbol{\nu} = r \in H^{-\frac{1}{2}}(\Gamma_N)$ on Γ_N,

where Γ_D and Γ_N form a partition for $\partial\Omega$, with $\Gamma_D \neq \emptyset$ and $\Gamma_N \neq \emptyset$.

In order to derive the weak formulation of the Richards problem, its rearranged version is considered:

$$\begin{cases} \underline{\underline{\boldsymbol{\kappa}}}^{-1}(\psi)\mathbf{q} + \boldsymbol{\nabla}\psi = -\boldsymbol{\nabla}z & \text{(37a)} \\ \partial_t\theta(\psi) + \boldsymbol{\nabla} \cdot \mathbf{q} = \hat{f} & \text{(37b)} \end{cases}$$

where $\underline{\underline{\boldsymbol{\kappa}}} = \underline{\underline{\mathbf{K}}}_{sat} k_{rw}$.

We start by multiplying Equation (37a) by $\mathbf{v} \in \mathbf{V}_0$ and Equation (37b) by $w \in Q$. By integrating over the domain Ω and exploiting the Gauss-Green formula [27], we derive the weak formulation for the Richards' equation:

$\forall t \in (0,T)$ *find* $(\mathbf{q}(t), \psi(t)) \in \mathbf{V} \times Q$ *such that:*

$$\begin{cases} \displaystyle\int_\Omega \underline{\underline{\boldsymbol{\kappa}}}^{-1}(\psi)\mathbf{q} \cdot \mathbf{v} - \int_\Omega \psi \boldsymbol{\nabla} \cdot \mathbf{v} = -\int_\Omega \boldsymbol{\nabla}z \cdot \mathbf{v} - \int_{\Gamma_D} s\mathbf{v} \cdot \boldsymbol{\nu} & \forall \mathbf{v} \text{ in } \mathbf{V}_0 \\ \displaystyle\int_\Omega \partial_t\theta(\psi)w + \int_\Omega w\boldsymbol{\nabla} \cdot \mathbf{q} = \int_\Omega \hat{f}w & \forall w \text{ in } Q \end{cases} \tag{38}$$

where, with an abuse of notation, we wrote $\langle \mathrm{tr}_{\boldsymbol{\nu}}\mathbf{v}, s\rangle_{\Gamma_D} = \int_{\Gamma_D} s\mathbf{v} \cdot \boldsymbol{\nu}$. The notation $\langle \cdot, \cdot\rangle_{\Gamma_D} : H^{-\frac{1}{2}}(\Gamma_D) \times H^{\frac{1}{2}}(\Gamma_D) \longrightarrow \mathbb{R}$ represents the duality operator between the two Sobolev spaces $H^{-\frac{1}{2}}(\Gamma_D)$ and $H^{\frac{1}{2}}(\Gamma_D)$. Notice that in our specific case, we have $s = 0 \ \forall n$.

4.1.2 Time Discretization of Richards' equation

As it can be easily observed, the Richards' equation is time dependent; hence, a time discretization procedure is needed in order to solve it numerically. Let $(0,T)$ denote the entire time span of interest and N_{ts} be the number of time steps. If we consider a uniform step length, we obtain that the single time step has a temporal length of $\Delta t = T/N_{ts}$. We can define a discrete sequence of time instants $\{t_n\}_{n=0}^{N_{ts}}$ such that $t_{n+1} = t_n + \Delta t$.

For the time discretization of the equation, we employ the Backward Euler discretization scheme. Even though it is computationally more demanding than an explicit scheme, it guarantees unconditional stability. Assuming $\mathbf{q}^{n+1}(\cdot) \approx \mathbf{q}(\cdot, t_{n+1})$ and $\psi^{n+1}(\cdot) \approx \psi(\cdot, t_{n+1})$, the discretized problem reads as follows:

Given $(\mathbf{q}_0, \psi_0) \in \mathbf{V} \times Q$, $\forall n = 0, ..., N_{ts} - 1$ *find* $(\mathbf{q}^{n+1}, \psi^{n+1}) \in \mathbf{V} \times Q$ *such that:*

$$
\begin{cases}
\displaystyle \int_\Omega \underline{\underline{\boldsymbol{\kappa}}}^{-1}(\psi^{n+1})\mathbf{q}^{n+1} \cdot \mathbf{v} - \int_\Omega \psi^{n+1}\boldsymbol{\nabla} \cdot \mathbf{v} = -\int_\Omega \boldsymbol{\nabla}z \cdot \mathbf{v} - \int_{\Gamma_D} s^{n+1}\mathbf{v} \cdot \boldsymbol{\nu} & \forall \mathbf{v} \text{ in } \mathbf{V}_0 \\[4mm]
\displaystyle \int_\Omega \frac{\theta(\psi^{n+1}) - \theta(\psi^n)}{\Delta t}w + \int_\Omega w\boldsymbol{\nabla} \cdot \mathbf{q}^{n+1} = \int_\Omega \hat{f}^{n+1}w & \forall w \text{ in } Q
\end{cases}
\tag{39}
$$

where $\hat{f}^{n+1} = \dfrac{\rho_i}{\rho_w}R_m W_{SSA}^{n+1}(T_{int}^{n+1} - T_{melt})$, with $W_{SSA}^{n+1} = S^{n+1}\dfrac{SSA_0}{\phi_0 ln(\phi_0)}\phi^{n+1}ln(\phi^{n+1})$ and $T_{int}^{n+1} = T_{int}(T_i^{n+1}, T_w^{n+1})$.

As we will see later in Section 4.3.2, the quantities S^{n+1}, ϕ^{n+1} and T_{int}^{n+1} are corrected iteratively.

4.1.3 Galerkin Method for Richards' equation

The Galerkin method is a numerical technique used to find approximate solutions for problems described by partial differential equations, where the idea is to reduce them to a system of algebraic equations [31]. To achieve this, we restrict the spaces $\mathbf{V}_0$ and Q for the test functions and exact solution to finite dimensional subspaces, namely $\mathbf{V}_{h,0} \subset \mathbf{V}_0$ and $Q_h \subset Q$, where we assumed that $\mathbf{V} = \mathbf{V}_0$.

Let $\{\boldsymbol{\varphi}_i\}_{i=0}^{N_h} \subset \mathbf{V}_{h,0}$ and $\{\xi_j\}_{j=0}^{M_h} \subset Q_h$ be the sets of basis functions for $\mathbf{V}_{h,0}$ and Q_h respectively, where $N_h = dim(\mathbf{V}_{h,0})$ and $M_h = dim(Q_h)$. According to the definition of basis function, we can approximate the exact solutions at time t_n $\mathbf{q}^n$ and ψ^n in System (39) as follows:

$$
\mathbf{q}^n \approx \mathbf{q}_h^n = \sum_{i=0}^{N_h} q_i^n \boldsymbol{\varphi}_i, \quad \psi^n \approx \psi_h^n = \sum_{j=0}^{M_h} \psi_j^n \xi_j,
\tag{40}
$$

where $\{q_i^n\}_{i=0}^{N_h}$, $\{\psi_j^n\}_{j=0}^{M_h} \subset \mathbb{R}$ are the *degrees of freedom*.

By applying the Galerkin method to Richards' equation we obtain:

Given $(\underline{\mathbf{q}}_0, \underline{\psi}_0) \in \mathbb{R}^{N_h} \times \mathbb{R}^{M_h}$, $\forall n = 0, ..., N_{ts} - 1$ *find* $(\{q_i^{n+1}\}_{i=0}^{N_h}, \{\psi_j^{n+1}\}_{j=0}^{M_h}) \in \mathbb{R}^{N_h} \times \mathbb{R}^{M_h}$ *such that:*

$$
\begin{cases}
\displaystyle \sum_{j=0}^{N_h} q_j^{n+1} \int_\Omega \underline{\underline{\boldsymbol{\kappa}}}^{-1}(\psi_h^{n+1})\boldsymbol{\varphi}_j \cdot \boldsymbol{\varphi}_i - \sum_{j=0}^{M_h} \psi_j^{n+1} \int_\Omega \xi_j\boldsymbol{\nabla} \cdot \boldsymbol{\varphi}_i = -\int_\Omega \boldsymbol{\nabla}z\boldsymbol{\varphi}_i - \int_{\Gamma_D} s^{n+1}\boldsymbol{\varphi}_i \cdot \boldsymbol{\nu} & \forall i = 0, ..., N_h \\[4mm]
\displaystyle \sum_{j=0}^{M_h} \int_\Omega \frac{\theta(\psi_h^{n+1})_j}{\Delta t}\xi_j\xi_i + \sum_{j=0}^{N_h} q_j^{n+1} \int_\Omega \xi_i\boldsymbol{\nabla} \cdot \boldsymbol{\varphi}_j = \int_\Omega \frac{\theta(\psi_h^n)}{\Delta t}\xi_i + \int_\Omega \hat{f}^{n+1}\xi_i & \forall i = 0, ..., M_h
\end{cases}
$$

where $\theta(\psi_h^n) = \displaystyle\sum_{j=0}^{M_h} \theta(\psi_h^n)\xi_j$.

As previously stated, employing this approach offers the advantage of formulating a linear system. The elements that make up the linear system are the following:

- $[M_q]_{ij} = \displaystyle\int_\Omega \underline{\underline{\boldsymbol{\kappa}}}^{-1}\boldsymbol{\varphi_j} \cdot \boldsymbol{\varphi_i}$ is the mass matrix for the Richards velocity $\mathbf{q}$,

- $[M_\psi]_{ij} = \displaystyle\int_\Omega \xi_j\xi_i$ is the mass matrix for the hydraulic pressure ψ,

- $[B]_{ij} = -\displaystyle\int_\Omega \xi_j\boldsymbol{\nabla} \cdot \boldsymbol{\varphi}_i$ is the divergence matrix,

- $[G]_i = -\displaystyle\int_\Omega \boldsymbol{\nabla}z\boldsymbol{\varphi}_i$ is the gravity term,

- $[\underline{F}^{n+1}]_i = \displaystyle\int_\Omega \hat{f}^n\xi_i$ represents the source term,

- $[\underline{BC}^{n+1}]_i = -\displaystyle\int_{\Gamma_D} s^{n+1}\boldsymbol{\varphi}_i \cdot \boldsymbol{\nu}$ accounts for boundary conditions,

- $\underline{q}^{n+1}$ and $\underline{\psi}^{n+1}$, which contain $\{q_i^{n+1}\}_{i=0}^{N_h}$ and $\{h_j^{n+1}\}_{j=0}^{M_h}$ respectively, are the unknowns.

With the elements just introduced, we assemble the following linear system and consequent Galerkin problem:
$Given\ (\mathbf{q}_0, \underline{\psi}_0) \in \mathbb{R}^{N_h} \times \mathbb{R}^{M_h}, \forall n = 0, ..., N_{ts} - 1\ \ find\ \ (\{q_i^{n+1}\}_{i=0}^{N_h}, \{\psi_j^{n+1}\}_{j=0}^{M_h}) \in \mathbb{R}^{N_h} \times \mathbb{R}^{M_h}\ such\ that:$

$$
\begin{bmatrix} 0 \\ \dfrac{M_h}{\Delta t}\underline{\theta}(\psi_h^{n+1}) \end{bmatrix} + \begin{bmatrix} M_q(\psi_h^{n+1}) & B^T \\ -B & 0 \end{bmatrix} \begin{bmatrix} \underline{q}^{n+1} \\ \underline{\psi}^{n+1} \end{bmatrix} = \begin{bmatrix} \underline{G} + \underline{BC}^{n+1} \\ \underline{F}^{n+1} + \dfrac{M_h}{\Delta t}\underline{\theta}(\psi_h^{n}) \end{bmatrix}
\tag{41}
$$

4.1.4 Treatment for the non linearity: the L-scheme

As already mentioned, Richards' equation is a nonlinear partial differential equation, where nonlinearities lie in the relations $\theta(\psi)$ and $\underline{\kappa}(\psi)$. Therefore, a linearization method must be introduced to treat these nonlinearities. Among various iterative methods, the L-scheme method, initially introduced by [26] and subsequently refined in works such as [22, 29, 30], is favored in this scenario. This preference arises from its capability to avoid the direct utilization of the derivative of $\theta(\psi)$ within the iterative solver at each iteration. Specifically, it differs from methods such as the Newton Method, where the entire iterative solver relies on the explicit employment of the Jacobian. In our approach, we determine the value for L by computing $\theta'(\psi)$ not at every iteration, but rather at each time step (see Section 4.3.2). This decision is specifically driven by the characteristics of the chosen groundwater model, which entails dealing with sharp and steep curves.

This method involves performing a Taylor expansion for $\theta(\psi)$ with respect to ψ, centered at ψ_k^{n+1}, which reads:

$$
\theta(\psi^{n+1}) \approx \theta(\psi_k^{n+1}) + L^n(\psi_{k+1}^{n+1} - \psi_k^{n+1})
\tag{42}
$$

where $L^n > 0$. Regarding the conductivity, it is treated adopting the idea behind the Picard method, where $\underline{\kappa}(\psi^{n+1}) \approx \underline{\kappa}(\psi_k^{n+1})$.

Convergence is ensured under the following conditions [22]:
1. The function for the moisture content $\theta(\cdot)$ must be monotone, Lipschitz continuous and $\theta'(\psi) \geq 0$,
2. The hydraulic conductivity $\underline{\kappa}$ must be L_ω-Lipschitz continuous, positive and bounded by κ_m,
3. It must be that $\max||\mathbf{q}_h^n|| < \gamma < +\infty$ and $\max||\boldsymbol{\nabla}\psi_h^n|| < \gamma < +\infty$,
4. $\frac{2}{L_\Theta} - \frac{1}{L}\Delta t\frac{(\gamma+1)^2 L_\omega^2}{\kappa_m} \geq 0$ with $L_\Theta = \sup_h \left| \frac{\partial\theta}{\partial\psi}(\psi) \right|$.

Let's concisely prove condition 1 for the specific problem addressed in this thesis. When examining the relationship expressed in Equation (19), we can easily compute its derivative as follows:

$$
\theta(\psi) = \begin{cases} (n-1)\alpha(-\alpha\psi)^{n-1}\dfrac{\theta_s - \theta_r}{[1 + (-\alpha\psi)^n]^{\frac{2n-1}{n}}} & \text{if } \psi \leq 0 \\ 0 & \text{if } \psi > 0 \end{cases}
\tag{43}
$$

The typical graphical representation for $\theta'(\psi) \cdot \mathbb{I}_{\psi \leq 0}$ for some values of α and n can be observed in Figure 4:
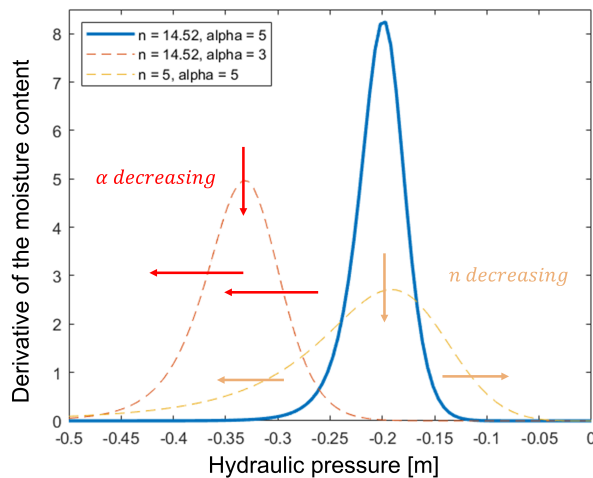

Figure 4: Shape of $\theta'(\psi)$ for different values of α and n.

where it can be easily observed that $\theta'(\psi) \longrightarrow 0$ for both $\psi \longrightarrow 0$ and $\psi \longrightarrow -\infty$, $\forall\alpha, n$. In addition, it is evident that it is continuous and bounded $\forall\psi$, which leads to the lipschitzianity property for θ. Moreover, it

can be observed that θ is monotonically increasing, being θ' strictly positive. Specifically, a decrease in α and n results in a reduced maximum steepness for θ.

Similar straightforward and visual reasoning can be applied to address point 2. Condition 3 is met as we employing relationships that are free from discontinuities and, in general, holds true in the absence of significant spatial heterogeneities. Under the same assumptions, point 4 is guaranteed (see [22]).

Applying the L-scheme method to System (39), a single iteration reads:

$$
\begin{cases}
\left(\underline{\underline{\kappa}}^{-1}(\psi_k^{n+1})\mathbf{q}_{k+1}^{n+1}, \mathbf{v}\right)_\Omega - \left(\psi_{k+1}^{n+1}, \boldsymbol{\nabla}\cdot\mathbf{v}\right)_\Omega = -\left(\boldsymbol{\nabla}z, \mathbf{v}\right)_\Omega - \left(s^{n+1}, \mathbf{v}\cdot\boldsymbol{\nu}\right)_{\Gamma_D} \\
\left(\theta(\psi_k^{n+1}), w\right)_\Omega + L\left(\psi_{k+1}^{n+1} - \psi_k^{n+1}, w\right)_\Omega + \Delta t(\boldsymbol{\nabla}\cdot\mathbf{q}_{k+1}^{n+1}, w)_\Omega = (\theta(\psi^n), w)_\Omega + \Delta t(\hat{f}_k^{n+1}, w)_\Omega
\end{cases}
\tag{44}
$$

where, to make the scheme clearer, the notation $(z,m)_\Omega = \int_\Omega zm$ and $(z,m)_{\Gamma_D} = \int_{\Gamma_D} zm$ is adopted.

Finally, by performing the Galerkin discretization of System (44), and by assuming $\underline{q}_0^{n+1} = \underline{q}^n, \underline{\psi}_0^{n+1} = \underline{\psi}^n \, \forall n = 0, ..., N_{ts} - 1$, we obtain the following problem:

$\forall n = 0, ..., N_{ts} - 1 \;\; find \;\; (\underline{q}^{n+1}, \underline{\psi}^{n+1}) \in \mathbb{R}^{N_h} \times \mathbb{R}^{M_h} \;\; such \; that:$

$$
\begin{bmatrix} M_q(\psi_k^{n+1}) & B^T \\ -\Delta t B & L M_\psi \end{bmatrix} \begin{bmatrix} \underline{q}_{k+1}^{n+1} \\ \underline{\psi}_{k+1}^{n+1} \end{bmatrix} = \begin{bmatrix} \underline{G} + \underline{BC}^{n+1} \\ L M_\psi \psi_k^{n+1} + \underline{\Theta}^n - \underline{\Theta}_k^{n+1} + \Delta t \underline{F}^{n+1} \end{bmatrix} \quad \forall k = 1, ..., K
\tag{45}
$$

where $\underline{\Theta}_k^{n+1} = M_\psi \underline{\theta}(\psi_k^{n+1})$, $\underline{\Theta}^n = M_\psi \underline{\theta}(\psi^n)$ and K represents the maximum number of iterations granted to the nonlinear solver.

4.1.5 Mixed Finite Element Method

For space discretization we employ the Mixed Finite Element method.

Let $\mathcal{T}_h$ be a triangulation for $\overline{\Omega}$, where $h = \frac{1}{N}$ and N is the mesh refinement. In particular, we have $2N^2$ elements per unit square. The triangulation $\mathcal{T}_h$ is such that [27]:

- $\overline{\Omega} = \bigcup_{K \in \mathcal{T}_h} K$;
- $\dot{K} \neq 0 \; \forall K \in \mathcal{T}_h$;
- $\dot{K}_i \cap \dot{K}_j = \emptyset, \; \forall K_i, K_j \in \mathcal{T}_h, \; i \neq j$;

where K_i is the i-th triangular element of the computational domain.

The Mixed Finite Element Method (MFEM) stipulates that the finite-dimensional subspaces mentioned in Section 4.1.3 for approximating the solution are constructed using piecewise polynomial functions.

We introduce Q_h as the space containing piece-wise constant functions, defined as in [10] as:

$$
Q_h := \mathbb{P}^0(\mathcal{T}_h) = \{p \in L^2(K) : \forall K \in \mathcal{T}_h, \, p|_K = \text{const} \in \mathbb{R}\}
$$

Since each element $p \in Q_h$ can be trivially expressed as a linear combination of unit functions over every element $K \in \mathcal{T}_h$, the basis functions for the $\mathbb{P}^0$ space may take on the following form:

$$
\xi_j = \frac{\mathbb{I}_{K_j}}{|K_j|}
$$

where $\mathbb{I}_{K_j}$ is the characteristic function for K_j and $|K_j|$ represents the volume of the specified element K_j [27]. Slightly more challenging is the formulation for $\mathbf{V}_h$ since the degrees of freedom are now associated with the edges of the cell rather than its center. The space of order zero Raviart-Thomas functions $\mathbb{RT}^0(\mathcal{T}_h)$ is chosen, whose expression reads [10]:

$$
\mathbb{RT}^0(\mathcal{T}_h) = \{\mathbf{q} \in H_{\boldsymbol{\nabla}\cdot}(\Omega) : \forall K \in \mathcal{T}_h \, \mathbf{q}|_K \in \mathbb{P}^0(K) + \mathbf{x}\mathbb{P}^0\}.
$$

To establish the basis functions for $\mathbb{RT}^0(\mathcal{T}_h)$, it is essential for us to make specific observations:

- Every internal edge is shared between two elements of $\mathcal{T}_h$;
- Three functions must be associated to every element, where φ_i is associated to the edge E_i of K.

As stated in [1], a suitable choice for basis functions in $\mathbb{RT}^0(\mathcal{T}_h)$ is provided by:

$$
\boldsymbol{\varphi}_{K,E_i}(\mathbf{x}) = \frac{\mathbf{x} - \mathbf{x}_{op,i}}{|K|}
$$

where $\mathbf{x}_{op,i}$ denotes the vertex situated opposite to the edge E_i. Note that

$$
\boldsymbol{\nabla}\cdot\boldsymbol{\varphi}_{K,E_i} = \frac{1}{|K|}, \, \forall i \quad \boldsymbol{\varphi}_{K,E_i}\cdot\mathbf{n}_j|_{E_j} = \frac{1}{|K|}\delta_{E_i,E_j} \qquad (\delta_{E_i,E_j} = 1 \text{ if } E_i = E_j)
$$

Ice equation		Water equation	
Term	Discretization	Term	Discretization strategy
$T_i T_{melt}$	$T_i^{n+1} T_{melt}$	$T_i T_{melt}$	$T_i^{n+1} T_{melt}$
$T_w T_{melt}$	$T_w^{n+1} T_{melt}$	$T_w T_{melt}$	$T_w^{n+1} T_{melt}$
$T_i T_i$	$T_i^{n+1} T_i^{n+1}$	$T_i T_i$	$T_i^{n+1} T_i^{n+1}$
$T_w T_w$	$T_w^{n+1} T_w^{n+1}$	$T_w T_w$	$T_w^{n+1} T_w^{n+1}$
$T_w T_i$	$T_w^{n+1} T_i^{n+1}$	$T_i T_w$	$T_i^{n+1} T_w^{n+1}$

Table 2: Implicit approach for the rhs. The terms in blue are corrected iteratively.

A visual depiction of the basis functions is presented in Figure 5:
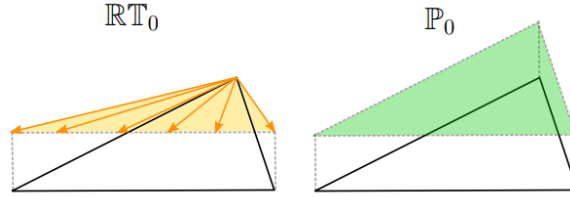
Figure 5: Basis functions for the $\mathbb{RT}^0$ and $\mathbb{P}^0$ spaces [1].

This approach is best suited for triangular meshes and proves particularly effective for problems where there might be notable variations in the order of magnitude of the coefficients.

4.2. Discretization of Thermal Energy Equations

The purpose of this section is to address the advection-diffusion-reaction equations outlined in Section 3.4 and perform discretization in both time and space over a computational domain. Similarly to the previous case, the goal is to formulate an algebraic system, and this is accomplished through the effective application of the Finite Volume Method.

4.2.1 Time discretization

Consider the thermal budget evolution equations (24), (25) presented in Section 3.4. They are clearly time dependent, hence, like for Richards' equation, a time discretization scheme is needed in order to solve them numerically.

Let $(0, T)$ denote the entire time span of interest and N_{ts} be the number of time steps. Again, the single time step has a length of $\Delta t = T/N_{ts}$. We can define a discrete sequence of time instants $\{t_n\}_{n=0}^{N_{ts}}$ such that $t_{n+1} = t_n + \Delta t$.

To discretize the equations in time, the Backward Euler discretization scheme is employed for the diffusion and transport terms. Concerning the source/sink term on the right-hand side, it is composed of the product between $T_{int} \propto \lambda_1 T_i + \lambda_2 T_w$, and $\alpha_\gamma \propto \dfrac{T_{int} - T_\gamma}{z_1(T_{int} - T_\gamma) + z_2(T_{int} - T_\delta)}$, resulting in evident non linear terms. The strategy is the following: once expanded, the denominator is corrected iteratively to avoid challenging inverse nonlinearities, whereas the products at the numerator are handled as shown in Table 2. Specifically, the blue terms are adjusted iteratively. This approach, which enforces the coupling between the two equations through cross terms, is selected among other possibilities to simplify the subsequent spatial discretization process.

Finally, the quantities ϕ, S, and $\mathbf{q}$ are already computed at time $n+1$, as outlined by the Richards'-thermodynamics coupling strategy presented in Algorithm 1. However, Richards' problem implicitly depends on the temperatures: details on the treatment of this coupling will be given in Section 4.3.2.

Assuming $T_\gamma^{n+1}(\cdot) \approx T_\gamma(\cdot, t_{n+1})$, the discretized problem reads as follows:

Given $(T_{i,0}, T_{w,0}) \in \mathbb{V}_h \times \mathbb{V}_h \ \forall n = 0, ..., N_{ts} - 1 \ \ find \ \ (T_i^{n+1}, T_w^{n+1}) \ \ such \ that:$

$$\rho_i c_i (1 - \phi^{n+1}) \left[\frac{T_i^{n+1} - T_i^n}{\Delta t} \right] - \boldsymbol{\nabla} \cdot (K_i (1 - \phi^{n+1}) \boldsymbol{\nabla} T_i^{n+1}) + \Lambda_i^{n+1} (T_{11}^{n+1} T_i^{n+1} + T_{12}^{n+1} T_w^{n+1}) =$$
$$= -\Lambda_i^{n+1} C_1 (C_2 + C_3) T_{melt}^2, \tag{46}$$

$$\rho_w c_w \left[\frac{\phi^{n+1} S^{n+1} (T_w^{n+1} - T_w^n)}{\Delta t} + \boldsymbol{\nabla} \cdot (\mathbf{q}^{n+1} T_w^{n+1}) \right] - \boldsymbol{\nabla} \cdot (K_w \phi^{n+1} S^{n+1} \boldsymbol{\nabla} T_w^{n+1}) +$$
$$+ \Lambda_w^{n+1} (T_{21}^{n+1} T_i^{n+1} + T_{22}^{n+1} T_w^{n+1}) = -\Lambda_w^{n+1} C_1 (C_2 + C_3) T_{melt}^2, \tag{47}$$

where the coefficients are defined as follows:

$$\Lambda_\gamma^{n+1} = -\frac{K_\gamma}{r_\gamma} \frac{\rho_w L_{sol} R_m W_{SSA}^{n+1}}{\frac{K_i}{r_i}(T_{int}^{n+1} - T_i^{n+1}) + \frac{K_w}{r_w}(T_{int}^{n+1} - T_w^{n+1})} \frac{1}{(C_1 + C_2 + C_3)^2}, \tag{48}$$

with

$$C_1 = \frac{c_w}{L_{sol}}, \quad C_2 = \frac{\beta_{sol} K_i}{\rho L_{sol} r_i}, \quad C_3 = \frac{\beta_{sol} K_w}{\rho L_{sol} r_w}$$

and

$$T_{11}^{n+1} = C_2 C_1 T_{melt} + (C_1 + C_3)(C_2 + C_3) T_{melt} - C_2 (C_1 + C_3) T_i^{n+1},$$
$$T_{12}^{n+1} = C_1 C_3 T_{melt} - C_3 (C_1 + C_3) T_i^{n+1} - C_3 (C_2 + C_3) T_{melt} + C_3 C_2 T_i^{n+1} + C_3 C_3 T_w^{n+1},$$
$$T_{21}^{n+1} = C_1 C_2 T_{melt} - C_2 (C_2 + C_3) T_{melt} + C_2 C_2 T_i^{n+1} + C_2 C_3 T_w^{n+1} - C_2 (C_1 + C_2) T_w^{n+1},$$
$$T_{22}^{n+1} = C_3 C_1 T_{melt} + (C_1 + C_2)(C_2 + C_3) T_{melt} - (C_1 + C_2) C_3 T_w^{n+1}.$$

As mentioned earlier, the denominator in Λ_γ^{n+1} and the T_{11}^{n+1}, T_{12}^{n+1}, T_{21}^{n+1}, T_{22}^{n+1} coefficients are computed using values at the previous iteration (see Algorithm 1).
We can now proceed with the spatial discretization.

4.2.2 Space Discretization with the Finite Volume Method

The Finite Volume Method is widely employed for the spatial discretization of partial differential problems in conservation form [21]. In particular, it is a method that can be used with any kind of polygonal mesh, in contrast to the Finite Element Method described in Section 4.1.5. However, for convenience, we will use the same grid as for the Richards' problem. In addition, to implement this method, variational techniques, such as deriving weak formulations, are not employed. Instead, the approach is primarily based on the conservation of physical quantities and the discretization of the domain into *control volumes*. The key component involves the definition of fluxes across the faces of these volumes.

Consider the domain Ω discretized by a triangulation $\mathcal{T}_h$ with identical characteristics to the triangulation defined in Section 4.1.5. We choose the finite dimensional space $\mathbb{V}_h = \{v \in L^2(\Omega) : v|_K = \text{const} \ \forall K \in \mathcal{T}_h\}$ of piecewise constant functions, with $\dim(\mathbb{V}_h) = M_h$. This choice implies that the approximation of the *conserved* variables T_i and T_w is considered constant within each control volume K [3]. The *cell-center* method is adopted, where the unknowns are associated to the barycenter of every control volume of $\mathcal{T}_h$ [27].

Now, considering the integration over a control volume $K \in \mathcal{T}_h$ and applying the Divergence Theorem, the transport term in Equation (47) con be reformulated as:

$$\int_{\partial K} \mathbf{q}^{n+1} T_w^{n+1} \cdot \mathbf{n} = \int_{\partial K} \mathbf{f}^{n+1}(T_w^{n+1}) \cdot \mathbf{n} = \sum_{\sigma \in \mathcal{E}_K} \int_\sigma \mathbf{f}^{n+1}(T_w^{n+1}) \cdot \mathbf{n}_\sigma = \sum_{\sigma \in \mathcal{E}_K} \mathbf{F}_{K,\sigma}^{n+1}(T_{w,K}^{n+1}, T_{w,L}^{n+1}) \cdot \mathbf{n}_\sigma |\sigma| \tag{49}$$

where $\mathcal{E}_K$ represents the set of edges of K and $\mathbf{n}_\sigma$ is the normal of the face $\sigma \in \mathcal{E}_K$ pointing towards cell L, being L the cell that shares the face σ with K. Moreover, $\mathbf{F}_{K,\sigma}^{n+1}(T_{w,K}^{n+1}, T_{w,L}^{n+1})$ is the numerical flux at time $n+1$ from cell K to cell L. It can be observed that if σ is an edge shared by K and L, then $\mathbf{F}_{K,\sigma} + \mathbf{F}_{L,\sigma} = 0$, which represents the conservativity of the fluxes.

Since the quantity $\mathbf{q}$ is given, the sign of $\mathbf{f}'(T_w)$ does not change with T_w. Consequently, to assign a value to $\mathbf{F}_{K,\sigma}$, the *upwind* scheme can be employed. By adopting this strategy, we obtain the following approximation for $\mathbf{F}_{K,\sigma}^{n+1}(T_{w,K}^{n+1}, T_{w,L}^{n+1})$:

$$\mathbf{F}_{K,\sigma}^{n+1}(T_{w,K}^{n+1}, T_{w,L}^{n+1}) \approx \mathbf{f}(T_{w,B}^{n+1})$$

where

$$B = \begin{cases} K & \text{if } \mathbf{q} \cdot \mathbf{n}_\sigma > 0, \\ L & \text{if } \mathbf{q} \cdot \mathbf{n}_\sigma < 0. \end{cases}$$

Now, let's investigate the discretization approach for the diffusive term. Once more, taking into account the integration over an element $K \in \mathcal{T}_h$, the diffusion term in Equation (46), (47) can be expressed as:

$$\int_{\partial K} \boldsymbol{\nabla} T_i^{n+1} \cdot \mathbf{n} = \int_{\partial K} \mathbf{g}(T_i^{n+1}) \cdot \mathbf{n} = \sum_{\sigma \in \mathcal{E}_K} \int_\sigma \mathbf{g}(T_i^{n+1}) \cdot \mathbf{n}_\sigma = \sum_{\sigma \in \mathcal{E}_K} \mathbf{G}_{i_{K,\sigma}}(T_{i,K}^{n+1}, T_{i,L}^{n+1}) \mathbf{n}_\sigma |\sigma| \tag{50}$$

$$\int_{\partial K} \boldsymbol{\nabla} T_w^{n+1} \cdot \mathbf{n} = \int_{\partial K} \mathbf{g}(T_w^{n+1}) \cdot \mathbf{n} = \sum_{\sigma \in \mathcal{E}_K} \int_\sigma \mathbf{g}(T_w^{n+1}) \cdot \mathbf{n}_\sigma = \sum_{\sigma \in \mathcal{E}_K} \mathbf{G}_{w_{K,\sigma}}(T_{w,K}^{n+1}, T_{w,L}^{n+1}) \mathbf{n}_\sigma |\sigma| \tag{51}$$

where $\mathbf{n}_\sigma$ is the outward normal of the face $\sigma \in \mathcal{E}_K$ and $\mathbf{G}_{\gamma_{K,\sigma}}$ is the numerical flux at time $n+1$ for phase γ from cell K to cell L. It can be observed that if σ is an edge between two cells K and L, then $\mathbf{G}_{\gamma_{K,\sigma}} + \mathbf{G}_{\gamma_{L,\sigma}} = 0$ $\forall \gamma$, which represents the conservativity of the fluxes. The idea is to adopt a strategy to approximate $\mathbf{G}_\gamma^{n+1}$ consistently.
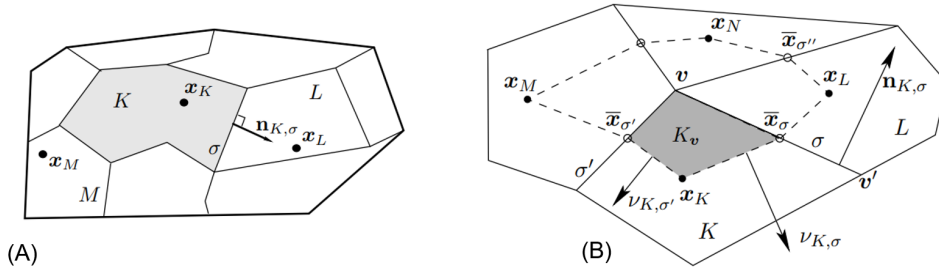
Figure 6: (A) TPFA, (B) MPFA (from [9]).

The chosen methodology entails the approximation of $\mathbf{G}_{\gamma_{K,\sigma}}$ by means of an enhanced version of the *Two-Point Flux Approximation (TPFA)* method, specifically the *Multi-Point Flux Approximation (MPFA)* method. Both strategies are expounded in greater detail in [9].

The *TPFA* method, in essence, determines the normal gradient through an edge σ by employing the approximated values of the conserved quantities evaluated at the centers of the two neighboring cells $\mathbf{x}_K$ and $\mathbf{x}_L$, as illustrated in Figure 6.A. It's crucial to emphasize that the quadrilaterals illustrated in Figure 6 are employed solely for graphical representation and do not accurately depict the actual triangulation $\mathcal{T}_h$. The main limitation of the *TPFA* method is its lack of adaptability to general grid types.

To overcome this limitation, a practical alternative is the *MPFA* method, which imposes no restrictions on the mesh choice. Specifically, this method assumes that the solution is piecewise linear in certain sub-cells around each vertex. It introduces additional edge unknowns to express the linear variation of the solution, allowing the computation of gradients and consequently fluxes in these sub-cells. The edge unknowns are then eliminated through interpolation using cell unknowns, and the conservation equations for its fluxes are formulated. The final numerical fluxes are expressed exclusively in terms of cell unknowns [9].

Let's consider the 2D case. For each edge σ, we fix its midpoint $\overline{\mathbf{x}}_\sigma$. Subsequently, at every vertex $\mathbf{v}$ on the grid, an *interaction region* is constructed by connecting the cell centers of a general element $\mathbf{x}_K$ surrounding $\mathbf{v}$ and the midpoints $\overline{\mathbf{x}}_\sigma$ of the edges which contain $\mathbf{v}$ (see Figure 6.B). This interaction region consists of a distinct sub-cell $K_\mathbf{v}$ for each cell K, and the solution is approximated using a function that exhibits linearity within each sub-cell surrounding $\mathbf{v}$.

By assuming continuity of this piecewise linear approximation at $\overline{\mathbf{x}}_\sigma$, after some computations, we obtain

$$\mathbf{G}_{\gamma_{K,\tau,\mathbf{v}}} \cdot \mathbf{n}_{K,\tau} = -d(\mathbf{v}, \overline{\mathbf{x}}_\tau) \boldsymbol{\nabla}_{K_\mathbf{v}} T_\gamma \cdot \mathbf{n}_{K,\tau}, \tag{52}$$

where $\boldsymbol{\nabla}_{K_\mathbf{v}} T_\gamma$ is constant, $d(\cdot, \cdot)$ is a distance, $\tau = \sigma, \sigma'$ and $\mathbf{n}_{K,\tau}$ denotes the unit outward normal vector from cell K along edge τ. Equation (52) denotes the sub-flux across the half edges $[\mathbf{v}\overline{\mathbf{x}}_\tau]$ around $\mathbf{v}$. The calculations leading to Equation (52) are thoroughly reported in [9].

To exclude the edge unknowns involved in the sub-fluxes, the conservation of the fluxes around $\mathbf{v}$ is imposed:

$\forall \tau$ such that $\mathbf{v} \in \tau$, if K, L are the cells that share edge τ, then

$$\mathbf{G}_{\gamma_{K,\tau,\mathbf{v}}} \cdot \mathbf{n}_{K,\tau} + \mathbf{G}_{\gamma_{L,\tau,\mathbf{v}}} \cdot \mathbf{n}_{L,\tau} = 0 \tag{53}$$

where $\mathbf{n}_{K,\tau} = -\mathbf{n}_{L,\tau}$ [9].

From the latter we derive a linear system on the edge unknowns $T_{\gamma,\sigma}$ and $T_{\gamma,\sigma'}$ around $\mathbf{v}$. This system is invertible, allowing us to express these edge unknowns in terms of the cell unknowns. By applying a similar procedure around the other vertex $\mathbf{v}'$ of σ, we can ultimately express the total flux through the edge σ of K as:

$$\mathbf{G}_{\gamma_{K,\sigma}} \cdot \mathbf{n}_{K,\sigma} = \mathbf{G}_{\gamma_{K,\sigma,\mathbf{v}}} \cdot \mathbf{n}_{K,\sigma} + \mathbf{G}_{\gamma_{K,\sigma,\mathbf{v}'}} \cdot \mathbf{n}_{K,\sigma} \tag{54}$$

where we exclusively involve the cell unknowns. By construction, $(\mathbf{G}_{K,\sigma})_{K \in \mathcal{T}_h, \sigma \in \mathcal{E}_k}$ satisfy the conservativity of the fluxes.

Finally, since the conserved quantities are assumed to be constant inside K, we can write

$$\int_K T_\gamma dK = T_\gamma \int_K dK = |K| T_\gamma \tag{55}$$

where $|K| = \int_K dK$ is the volume of element K.

In light of the earlier observations, the fully discretized form of Equations (24), (25) reads as follows:

Given $(\underline{T}_{i,0}, \underline{T}_{w,0}) \in \mathbb{V}_h \times \mathbb{V}_h, \forall n = 0, ..., N_{ts} - 1$ *find* $(\{T_{i,K}^{n+1}\}_{K \in \mathcal{T}_h}, \{T_{w,K}^{n+1}\}_{K \in \mathcal{T}_h}) \in \mathbb{V}^h \times \mathbb{V}^h$ *such that:*

$$\sum_{K \in \mathcal{T}_h} \rho_i c_i (1 - \phi^{n+1}) |K| \left[\frac{T_{i,K}^{n+1} - T_{i,K}^n}{\Delta t} \right] - \sum_{K \in \mathcal{T}_h} \left[K_i (1 - \phi^{n+1}) \sum_{\sigma \in \mathcal{E}_K} \mathbf{G}_{i_{K,\sigma}}(T_{i,K}^{n+1}, T_{i,L}^{n+1}) \cdot \mathbf{n}_{K,\sigma} |\sigma| \right] +$$

$$+ \sum_{K \in \mathcal{T}_h} \Lambda_{i,K}^{n+1} |K| (T_{K,11}^{n+1} T_{i,K}^{n+1} + T_{K,12}^{n+1} T_{w,K}^{n+1}) = - \sum_{K \in \mathcal{T}_h} |K| \Lambda_{i,K}^{n+1} C_1 (C_2 + C_3) T_{melt}^2, \tag{56}$$

$$\rho_w c_w \left[\sum_{K \in \mathcal{T}_h} \phi^{n+1} S^{n+1} |K| \frac{(T_{w,K}^{n+1} - T_{w,K}^n)}{\Delta t} + \sum_{K \in \mathcal{T}_h} \sum_{\sigma \in \mathcal{E}_K} \mathbf{F}_{K,\sigma}^{n+1}(T_{w,K}^{n+1}, T_{w,L}^{n+1}) \cdot \mathbf{n}_\sigma |\sigma| \right] +$$

$$- \sum_{K \in \mathcal{T}_h} \left[K_w \phi^{n+1} S^{n+1} \sum_{\sigma \in \mathcal{E}_K} \mathbf{G}_{w_{K,\sigma}}(T_{w,K}^{n+1}, T_{w,L}^{n+1}) \mathbf{n}_{K,\sigma} |\sigma| \right] + \sum_{K \in \mathcal{T}_h} \Lambda_{w,K}^{n+1} |K| (T_{K,21}^{n+1} T_{i,K}^{n+1} + T_{K,22}^{n+1} T_{w,K}^{n+1}) = \tag{57}$$

$$= - \sum_{K \in \mathcal{T}_h} |K| \Lambda_{w,K}^{n+1} C_1 (C_2 + C_3) T_{melt}^2,$$

where L is the cell that shares the edge σ with cell K, $\Lambda_{\gamma,K}^{n+1} = \Lambda_\gamma^{n+1}(T_{i,K}^{n+1}, T_{w,K}^{n+1})$ and $T_{K,MN}^{n+1} = T_{MN}^{n+1}(T_{i,K}^{n+1}, T_{w,K}^{n+1})$ $(M, N = 1, 2)$.

To make the notation slightly clearer, the matrix form of the problem is formulated as follows:

$\forall n = 0, ..., N_{ts} - 1$ *find* $(\underline{T}_i^{n+1}, \underline{T}_w^{n+1}) \in \mathbb{V}^h \times \mathbb{V}^h$ *such that:*

$$A^{n+1} \underline{T}^{n+1} = \underline{b}^{n+1} \tag{58}$$

where

$$A^{n+1} = \begin{bmatrix} A_{11}^{n+1} & A_{12}^{n+1} \\ A_{21}^{n+1} & A_{22}^{n+1} \end{bmatrix}$$

$$\underline{b}^{n+1} = \begin{bmatrix} \rho_i c_i (1 - \phi^{n+1}) M_i \underline{T}_i^n + \Delta t K_i (1 - \phi^{n+1}) \underline{d}_i + \Delta t |B| \underline{\Lambda}_i^{n+1} C_1 (C_2 + C_3) T_{melt}^2, \\ \rho_w c_w \phi^{n+1} S^{n+1} M_w \underline{T}_w^n + \Delta t K_w \phi^{n+1} S^{n+1} \underline{d}_w + \Delta t \rho_w c_w \underline{u}_{w,K}^{n+1} + \Delta t |B| \underline{\Lambda}_w^{n+1} C_1 (C_2 + C_3) T_{melt}^2 \end{bmatrix}$$

$$\underline{T}^{n+1} = \begin{bmatrix} \underline{T}_i^{n+1} \\ \underline{T}_w^{n+1} \end{bmatrix}$$

and

$$A_{11}^{n+1} = \rho_i c_i (1 - \phi^{n+1}) M_i + \Delta t K_i (1 - \phi^{n+1}) D_i + \Delta t \underline{\Lambda}_i^{n+1} M_i \underline{T}_{11}^{n+1},$$
$$A_{12}^{n+1} = \Delta t \underline{\Lambda}_i^{n+1} M_w \underline{T}_{12}^{n+1},$$
$$A_{21}^{n+1} = \Delta t \underline{\Lambda}_w^{n+1} M_i \underline{T}_{21}^{n+1},$$
$$A_{22}^{n+1} = \rho_w c_w \phi^{n+1} S^{n+1} M_w + \Delta t \rho_w c_w U_w^{n+1} + \Delta t K_w \phi^{n+1} S^{n+1} D_w + \Delta t \underline{\Lambda}_w^{n+1} M_w \underline{T}_{22}^{n+1},$$

with

$$\underline{T}_\gamma^{n+1} = \{T_{\gamma,K}^{n+1}\}_{K \in \mathcal{T}_h}, \quad \underline{T}_\gamma^n = \{T_{\gamma,K}^n\}_{K \in \mathcal{T}_h}$$
$$\underline{\Lambda}_\gamma^{n+1} = \{\Lambda_{\gamma,K}^{n+1}\}_{K \in \mathcal{T}_h},$$
$$\underline{T}_{MN}^{n+1} = \{T_{K,MN}^{n+1}\}_{K \in \mathcal{T}_h}.$$

Please note that the product $\underline{a}\,\underline{b}$ should be understood as component-wise multiplication and that the implicit terms in $\underline{\Lambda}_\gamma^{n+1}$ and $\underline{T}_{MN}^{n+1}$ are adjusted iteratively.

Specifically, M_γ represents the mass matrix for phase γ, D_γ addresses the diffusive term, and U_γ^{n+1} handles the transport term at time $n+1$. Additionally, $\underline{d}_\gamma$ and $\underline{u}_\gamma^{n+1}$ are associated with the boundary conditions applied to the diffusive and transport terms, respectively.

Being the transport term addressed implicitly, there is no imposition of a *Courant-Friedrichs-Lewy* (CFL) condition for temporal stability.

4.3. Details of the implementation

To implement this model, two Python libraries have been employed:
- *PorePy* [19]: for mesh generation, exporting processes, and assembly of Finite Volume method matrices.
- *PyGeoN* [11] (depending on *PorePy*): For the instantiation of $\mathbb{RT}^0$ and $\mathbb{P}^0$ classes, as well as the assembly of matrices for the Mixed Finite Element method.

The simulations are run on Ubuntu version 22.04.02 on a personal laptop (Intel(R) Core(TM) i7-8550U CPU @ 1.80GHz, 4 cores, RAM 32GB).

4.3.1 Domain and Grid

The aim is to implement the model in a physical domain in two dimensions, specifically representing a thin column extracted from a snowpack. In particular, we consider $\Omega = (0, 0.2)$ m $\times (0, 1)$ m (see Figure 7). The domain is discretized using a structured triangle grid, where the elementary cell is obtained from the splitting of squares along the diagonal. Maintaining a height-to-width ratio of 5, this proportion is consistently upheld in the number of triangular cells in both the x and z dimensions. For each 2D simulation (Test Cases 1, 2, 3, 4), we select $N = 20$ as mesh refinement.
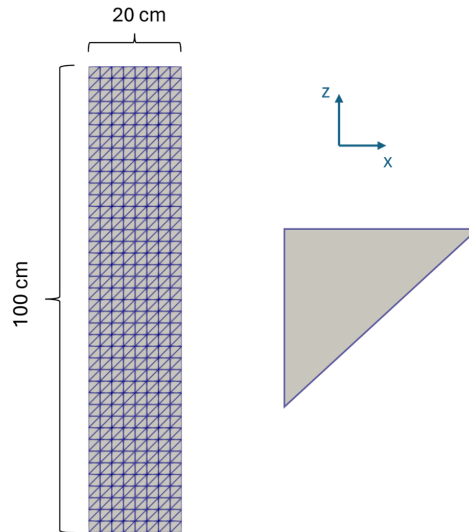
Figure 7: Discretized rectangular domain (left) and its elementary cell (right).

.

Until now, we have discussed boundaries labeled as the top, bottom and lateral boundary. Specifically, their respective analytical expressions are presented below:

$$\Gamma_t = \{(x, z) \in \partial\Omega \,|\, z = 1\},$$
$$\Gamma_b = \{(x, z) \in \partial\Omega \,|\, z = 0\},$$
$$\Gamma_l = \{(x, z) \in \partial\Omega \,|\, x = 0 \vee x = 0.2\}.$$

4.3.2 Splitting strategy

The outlined problem involves a strong coupling, specifically between the fluid dynamic aspect governed by Richards' equation and the thermodynamic process. While thermodynamics holds a crucial role in the definition of the sink term of the mass conservation equations (16), (17), the Darcy velocity, conversely, influences the transport term in the evolution equations (24), (25) for the temperature fields.

As previously mentioned in Section 4.1, the gravitational mechanics is solved monolithically utilizing the Mixed Finite Element method, where the nonlinearity in $\theta(\psi)$ and $\underline{\kappa}(\psi)$ is managed through L-scheme iterations (see Section 4.1.4). Regarding thermodynamics, solving the system represented by the evolution equations (24), (25) monolithically proves challenging due to the non-standard nature of the right-hand side assembly, which is highly nonlinear in $T_i, T_w, T_{int}(T_i, T_w)$.

The coupling among hydraulic pressure, flux, porosity and the two temperatures is enforced iteratively, with the nested iterations detailed in Algorithm 1. For every time step, it is essential to ensure the convergence of the Richards' system to obtain meaningful values for saturation and porosity (k-for loop). As S and ϕ are interdependent, they are iteratively adjusted in a dedicated short w-cycle, where only algebraic substitutions take place. Once the values of ψ, $\mathbf{q}$, S, and ϕ are obtained, they are then employed to solve the thermodynamics system. This process is iterated for each time step in the j-for loop.

Algorithm 1 Pseudocode

1: Initialization
2: **for** n in $0, ..., N_{ts}$ **do**
3:     Definition of $L^n = \max\limits_{\psi^n < 0} \theta^{n\prime}(\psi^n)$
4:     Definition of time-dependent rhs for Darcy and mass conservation equation
5:     **for** j in $0, ..., J$ **do**
6:        **for** k in $0, ..., K$ **do**
7:           Solve Richards using $S_{k,j}^{n+1}$, $\phi_{k,j}^{n+1}$, $T_{int,j}^{n+1}$
8:           **for** w in $0, ..., W$ **do**
9:              Update: $S_{w+1,j+1,k+1}^{n+1} = f(\psi_{k+1}^{n+1}, \phi_{w,j+1,k+1}^{n+1})$
10:          Update: $\phi_{w+1,j+1,k+1}^{n+1} = g(\phi_{w,j+1,k+1}^{n+1} S_{w+1,j+1,k+1}^{n+1}, T_{int,j}^{n+1})$
11:           **end for**
12:           # We have $S_{k+1,j+1}^{n+1}, \phi_{k+1,j+1}^{n+1}$
13:        **end for**
14:        # We have $q_{j+1}^{n+1}, \psi_{j+1}^{n+1}, S_{j+1}^{n+1}, \phi^{j+1}$
15:        Solve Thermodynamics using the above quantities and $T_{int,j}^{n+1}$
16:        Update: $T_{int,j+1}^{n+1} = h(T_{i,j+1}^{n+1}, T_{w,j+1}^{n+1})$
17:     **end for**
18:     # We have $q^{n+1}, \psi^{n+1}, S^{n+1}, \phi^{n+1}, T_i^{n+1}, T_w^{n+1}, T_{int}^{n+1}$
19:     Export $q^{n+1}, \psi^{n+1}, S^{n+1}, \phi^{n+1}, T_i^{n+1}, T_w^{n+1}, T_{int}^{n+1}$
20: **end for**

Specifically, in line 10 of Algorithm 1, we discretize and solve the ordinary differential equation stated in Equation (16) using a Backward Euler approach.

The stopping criterion for the $k-$loop is the following:

$$||\psi_{k+1}^{n+1} - \psi_k^{n+1}|| \leq \epsilon_a + \epsilon_r ||\psi_k^{n+1}||, \tag{59}$$

where $\epsilon_a = \epsilon_r = 10^{-6}$, $K = 30$, $J = 20$, $W = 3$ and $|| \cdot ||$ is the Euclidean norm.

Regarding the j-loop and w-loop, the criterion is similar to (59), with the variables of interest being T_i and S respectively.

Concerning the definition of L^n for the L-scheme, its selection holds crucial significance. While conventional practice often involves a constant value for L proportional to the maximum of $\theta'(\psi)$ throughout the entire process, this scenario favors a time-dependent variation for L. The significance of this choice becomes evident

in Figure 2, where, for $\psi \in [-0.3, -0.1]$, both $\theta(\psi)$ and $k_r(\psi)$ exhibit steep profiles, contrasting with the relatively flat shapes in the external intervals. This observation emphasizes the need to incorporate a time-dependent formulation for L, accounting for the most critical value of $\theta'(\psi)$ across the entire domain, namely, the highest one, for every considered time instant. This approach allows for faster convergence when the whole domain is characterized by ψ associated with the flat portions of θ and k_r. Simultaneously, as we approach the value for ψ where the models for θ and k_r exhibit high gradients, a suitable value of L is selected to guarantee convergence. Therefore, the selected explicit expression for L^n is as follows:

$$L^n = \max_{\psi^n < 0} \theta^{n'}(\psi^n).$$

5. Numerical Results

In this section, we present the results obtained from various conducted tests. With Test Case 0, we lay the groundwork for the analysis by presenting the preliminaries through a zero-dimensional analysis, while the subsequent tests are realized in two dimensions.

5.1. Test Case 0: zero-dimensional analysis

To deepen our understanding of the model and the associated quantities, we analyze zero dimensional experiments. The domain is confined to a single cell, where all the physical quantities are averaged over the REV (see Section 2.1), which corresponds to the same cell. This restriction results in a system of ordinary differential equations with respect to time, as we set the constraints $\frac{\partial}{\partial x} = \frac{\partial}{\partial y} = \frac{\partial}{\partial z} = 0$. The system of equations that arises, and its temporal discretization are presented in Appendix B.

5.1.1 Test 0/A: Low initial saturation

The simulation is run on a time period of $T = 2$ s, with $\Delta t = 0.01$ s and initial conditions $\phi_0 = 0.468$, $S_0 = 3 \times 10^{-3}$, $T_{i,0} = -5°C$, $T_{w,0} = 0°C$. In practical terms, the initial time is characterized by a minimal presence of water compared to air in the void space.
The temporal evolution of the quantities of interest is depicted in Figure 8:
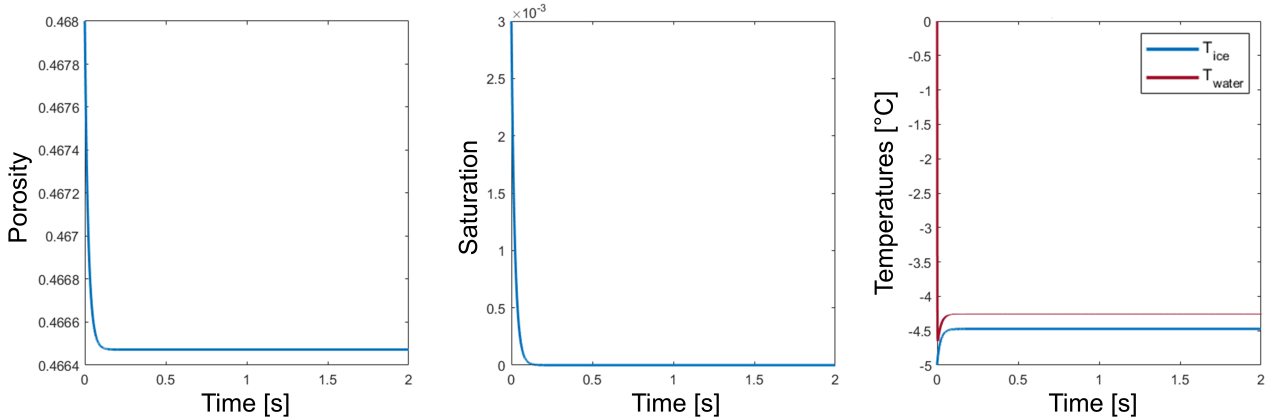
Figure 8: Temporal behaviour for Porosity ϕ, Saturation S, and Temperatures T_i, T_w.

It is evident that the small amount of water present in the snowpack undergoes complete refreezing, leading to a water saturation reaching zero. Coherently, the porosity decreases, indicating an increase in the mass of ice. The temperature of ice experiences a slight increase owing to the heat released by water during the freezing process. It eventually stabilizes at around $-4.5°C$, still significantly below the melting point. Conversely, assigning a precise meaning to water temperature becomes intricate as it progressively transforms into ice, and eventually, no water mass remains to be associated with a temperature. Hence, the temperature plot cannot be deemed descriptive for water, especially considering that we are dealing with averaged quantities at the Darcy scale.

5.1.2   Test 0/B: High initial saturation

The configuration remains consistent with that outlined in Section 5.1.1. The only change lies in the initial quantity of water in the cell, where the condition $S_0 = 0.2$ is now selected. This condition indicates that a substantial portion of the void space, namely 20%, is occupied by water.

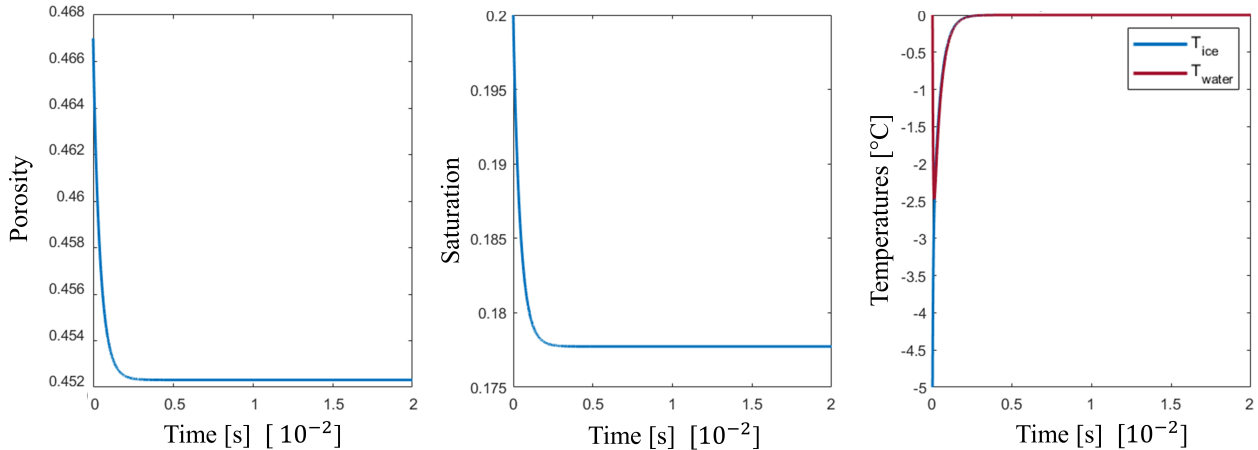Running the simulation reveals the following temporal behavior for the quantities of interest:

Figure 9: Temporal behaviour for Porosity ϕ, Saturation S, Temperatures T_i, T_w.

In this setting, the evident and istantaneous decrease in porosity and saturation indicates a significant transformation of water into ice during the initial time period. Specifically, the porosity transition from $\phi_0 = 0.468$ to $\phi \approx 0.452$ indicates a more pronounced refreezing phenomenon compared to the one observed in Section 5.1.1. This phase change can be attributed to the abundant availability of water for the process of refreezing. As the refreezing process unfolds, the ice absorbs the latent heat released by water, leading to a decrease in the temperature of the liquid phase during this brief period. Simultaneously, the significant amount of remaining water enables a relevant heat exchange between the two phases, albeit insufficient to induce additional phase changes. The temperatures tend to stabilize at the melting point, reflecting the coexistence of ice and the liquid water at the melting temperature, while maintaining their distinct phases. Notice that in the plots we have presented the curves corresponding to the first 0.02 seconds.

5.2.   Test Case 1: Total Refreezing

A more intriguing analysis is conducted by transitioning to a two dimensional domain and examining the dynamics of the phenomenon within a domain of the type described in Section 4.3.1. A mesh refinement $N = 20$ is chosen and the overall simulation length is $T = 2760$ s, with $\Delta t = 0.5$ s.

Regarding the boundary conditions, we refer to the general form discussed in Sections 3.3, 3.4. As for the fluid dynamic aspect, described by Richards' system, at the upper boundary, the constant natural condition is set to $\psi_{\text{top}} = 1$ m, in order to mimic the perpetual presence of a water source from above. Simultaneously, for the thermodynamic component, the temperature of ice at the bottom is subjected to the Dirichlet condition $T_{i,b} = -5°$C. The comprehensive set of imposed boundary conditions is, in practice, as follows:

$$
\begin{aligned}
\mathbf{q} \cdot \mathbf{n} = 0, \qquad & \boldsymbol{\nabla} T_i \cdot \mathbf{n} = 0, \qquad && \boldsymbol{\nabla} T_w \cdot \mathbf{n} = 0 \qquad && \text{on } \Gamma_l \\
\psi = 1, \qquad & T_i = T_{melt}, \qquad && T_w = T_{melt} \qquad && \text{on } \Gamma_t \\
\mathbf{q} \cdot \mathbf{n} = 0, \qquad & T_i = -5, \qquad && \boldsymbol{\nabla} T_w \cdot \mathbf{n} = 0 \qquad && \text{on } \Gamma_b
\end{aligned}
$$

where the conditions of heat fluxes already take into account that no advective flux is enforced on those boundaries.

Regarding the initial conditions, we opt for a uniform hydraulic pressure $\psi_0 = -0.3$ m, which is analytically linked to $S_0 \approx 0.0042$ through the model described in (19). The parameters α and n are consistent with those declared in Section 3.5. The initial porosity is set to $\phi_0 = 0.468$, whose spatial uniformity indicates a state of homogeneous snow. Finally, we initialize $T_{i,0} = -5°$C and $T_{w,0} = 0°$C. The initial water content within the snowpack at time $t = 0$ s is minimal, meaning that our investigation involves a relatively dry snowpack.

Consequently, we expect a behavior akin to the *0D* case, where only a marginal heat exchange between the phases is observed.

Our expectation is validated, indeed, starting the simulation with an initially low saturation results in a markedly reduced permeability across the entire domain. Specifically, at time $t = 0$ s, the domain exhibits an initial water relative permeability equal to 4.28×10^{-7}, posing significant hindrance to water infiltration from above. The outcome is that no infiltration is observed within the considered time span.

Figure 10 illustrates the evolution of saturation and porosity over time, with the time axis scaled logarithmically, at depths of 1 cm and 50 cm below the surface. In particular, Figure 10.A shows an abrupt decrease in saturation within the initial time steps ($\sim$ first 20 time steps) at the mid-domain level, rapidly diminishing to a residual saturation of 1×10^{-3}. This reduced saturation level persists throughout the entire simulation duration. In the early stages of the simulation, a pronounced refreezing process is indeed evident at the same quota, primarily due to the prevailing presence of *cold* ice rather than water. The transformation of water into a solid state is confirmed by the sudden reduction in porosity at the same quota, as illustrated in Figure 10.B. Solidification unequivocally contributes to an increase in ice mass and concurrently diminishes the available void space for water.

The scenario changes when observing the values just below the surface. Saturation decreases at a similar rate to the previously analyzed case but then suggests the beginning of an increasing trend, as highlighted in orange in Figure 10.A. Simultaneously, porosity, after the initial sudden decrease, continues to decrease.
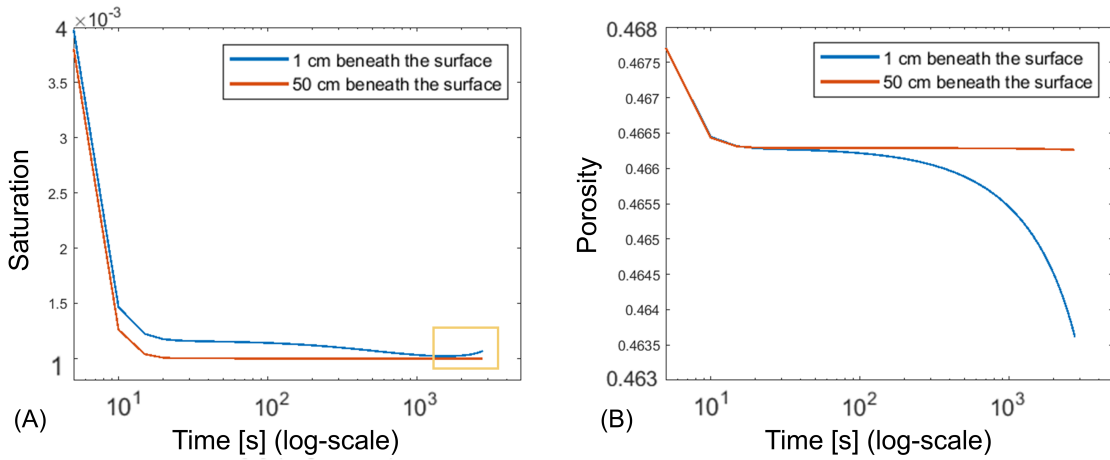
Figure 10: (A) Quota-averaged saturation, (B) Quota-averaged Porosity over time. Note the logarithmic scale on the abscissa.

These outcomes suggest the start of infiltration; however, refreezing occurs before actual water penetration in snow takes place. Nevertheless, the delayed increasing trend of saturation suggests that infiltration might begin to be observed in the future, with a very slow dynamics.

Moreover, observing the behavior of ice over time is significant. As depicted in Figure 11.A, ice experiences heat diffusion from the overlying water source. Specifically, the heat from above diffuses along the longitudinal axis of the snowpack, gradually warming the underlying layers. While Figure 11.A visualizes the actual phenomenon within the upper 10 cm of the snowpack for two different time instants, the same visualization is provided for water temperature in Figure 11.B, which shares the same kind of behaviour with the solid phase. Figure 11.C illustrates the value of ice and water temperatures along the entire central vertical axis for the same time instants. In this process of heat diffusion, water heats up more gradually as its specific heat capacity is higher than that of ice. This implies that, with an equivalent mass, a greater amount of heat is required to increase the temperature of water.

In this study, we have simulated only the initial 45 minutes of the phenomenon due to computational constraints, precluding an exploration of a longer time window. Nevertheless, the obtained outcome aligns with the trend presented in the results by [23] (pag. 13), where the outcome at the end of Day 0 is reported. In particular, the investigation carried out in [23] is one-dimensional and incorporates an additional term for Richards' equation. However, given its one-dimensional scope, the phenomenon it aims to model is identical to that of the present study. The results in [23] indicate that infiltration becomes noticeable starting from Day 12. Hence, we anticipate that this expected timing for observing infiltration also might apply in our case. As mentioned before, regrettably, simulating such a prolonged time span proves computationally expensive with the available resources. Increasing the time step is not a viable solution to this problem, as it results in the failure of convergence for Richards' equation.

As depicted in Figure 12(a), it is evident that, over time, the number of iterations required for the j-cycle, representing the iterations for the convergence of the thermodynamic problem, consistently diminishes throughout

the initial temporal steps. Note that the presented data is confined to the initial 50 time steps: notably, beyond that time, three iterations per time step are sufficient for the remaining part of the simulation.
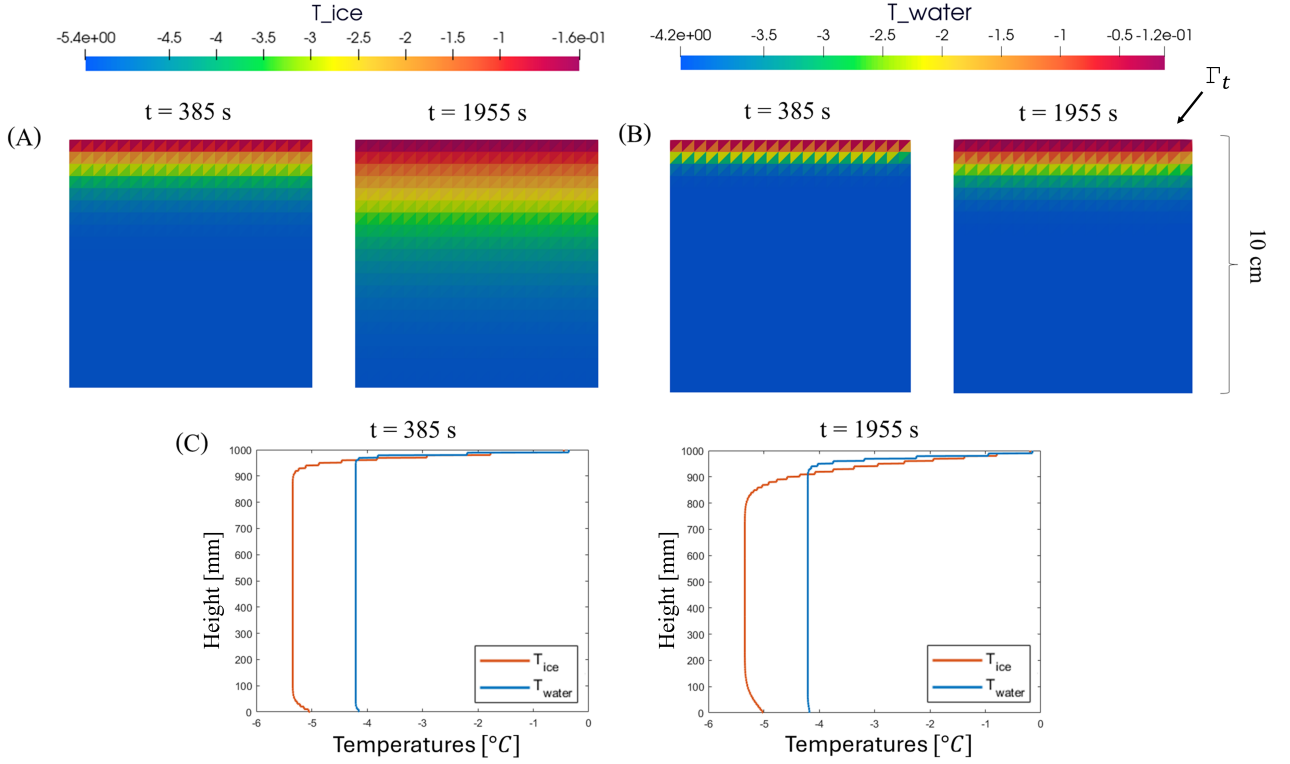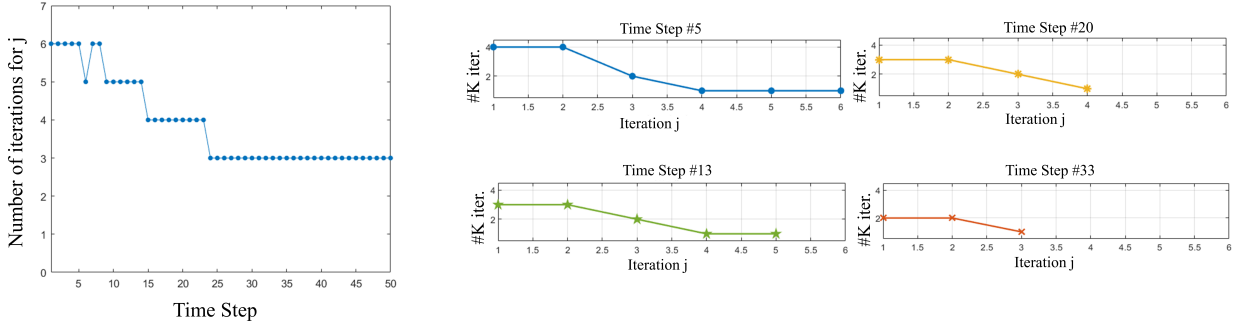

Figure 11: (A) T_i, (B) T_w for two different time instants, (C) Profile over T_i and T_w along the central vertical axis for the same time instants.

((a)) Number of iterations for the j-cycle per time step.

((b)) Number of iterations for the k-cycle per iteration j for four selected time steps.

Figure 12: Iteration count for Test Case 1.

The iteration count for the nonlinear solver employed in resolving Richards' equations is documented during the initial time steps in Figure 12(b). The number of iterations is relatively small and decreases as the simulation progresses over time. The modest number of Richards' iterations from the outset may be attributed to the absence of significant dynamics in terms of flux and pressure.

5.3.   Test Case 2: Uniform Infiltration

The second type of test aims to observe the actual infiltration of water from the top. To induce such a phenomenon, the initial condition for hydraulic pressure is set to $\psi_0 = -0.22$ m, corresponding to $S_0 \approx 0.223$. In this scenario, the value of $k_r(\psi)$ is relatively high from the beginning ($k_r \approx 0.07$), indicating a considerably higher overall conductivity compared to the scenario outlined in Test Case 1 (K_s remains constant). This

increased permeability facilitates a more straightforward flow of water through the porous medium. The overall simulation length is $T = 118$ s, with $\Delta t = 0.025$ s.

The boundary conditions remain consistent with those set for Test Case 1, as well as for the homogeneous initial conditions for ϕ, T_i, T_w.

Figure 13.A depicts the mechanics of uniform infiltration from above at different time instants. The variable of interest is the *liquid water content* (LWC), expressed as the percentage associated with the moisture content $\theta = S\phi$. It can be observed that the problem is symmetric, however the solution is not. This slight asymmetry is solely attributable to the fact that the employed mesh possesses a preferential direction and orientation, thus preventing pure uniform infiltration. This slight asimmetry is noticeable, for instance, at $t = 9.3$ s. A careful visual examination of Figure 13.A for $t = 117.45$ s unveils an accumulation of liquid water content at the bottom. This aligns with expectations, as unfrozen water descends due to gravity along the domain, and concurrently, null flux is imposed at Γ_b. Simultaneously, Figure 13.B shows the profile of LWC along the central vertical axis of the domain.
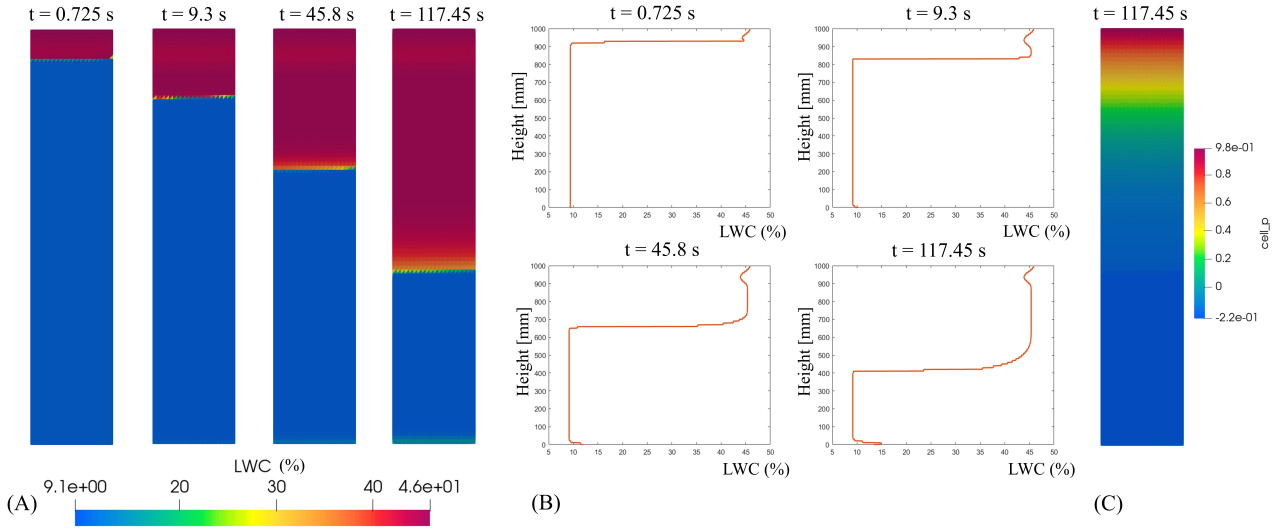
Figure 13: Uniform Infiltration. (A) LWC, (B) Profile of LWC along the central vertical axis with respect to z, (C) Hydraulic pressure gradient distribution for one time instant.

A reduction in porosity occurs when there is an exchange of heat between water and ice, allowing water to refreeze and integrate into the solid structure increasing the mass of ice. The magnitude of this process is directly proportional to the amount of water available for the exchange. Naturally, the more water at 0°C, the faster the ice will reach equilibrium with water, as the process redistributes a portion of the heat to the solid structure. Concurrently, there is an increased availability of liquid phase that has the potential to undergo refreezing, as long as the ice remains below the melting point.

Figure 14 depicts the diminishing trend over time of the porosity averaged across two distinct zones. Zone A characterizes the region where heat exchange takes place between ice and the <u>initial</u> water within the void space. Regarding changes in porosity, the infiltration process does not impact this zone. In fact, once the infiltration front reaches the upper section of Zone A, ice has already achieved equilibrium through heat exchange with the initial mass of water within the snowpack, resulting in modest refreezing. This prevents any additional phase changes from taking place.

Zone B denotes the region where a significant alteration in porosity takes place at the beginning of infiltration, indeed here, from the initial moments, we observe the coexistence of ice and water at varying temperatures, alongside an abundant presence of water. The mentioned observations provide a justification for the presence of an undershoot in LWC just beneath the surface depicted by Figure 13.B. Specifically, the porosity in this area attains the value of $\phi = 0.44$.

Moreover, Figure 13.C depicts the distribution of pressure for one time instant. The infiltration rate is not constant, as it can be qualitatively observed from the position of the front for the four time instants presented in Figure 13.A. As a matter of fact, infiltration rate tends to decrease over time. This is because, as time passes, the gradient of the pressure of the water phase at the infiltration front decreases. Water infiltrating does not experience the same pressure gradient imposed at the top boundary; instead, the gradient of pressure at the front diminishes as it descends, resulting in a progressively reduced intensity of infiltration.
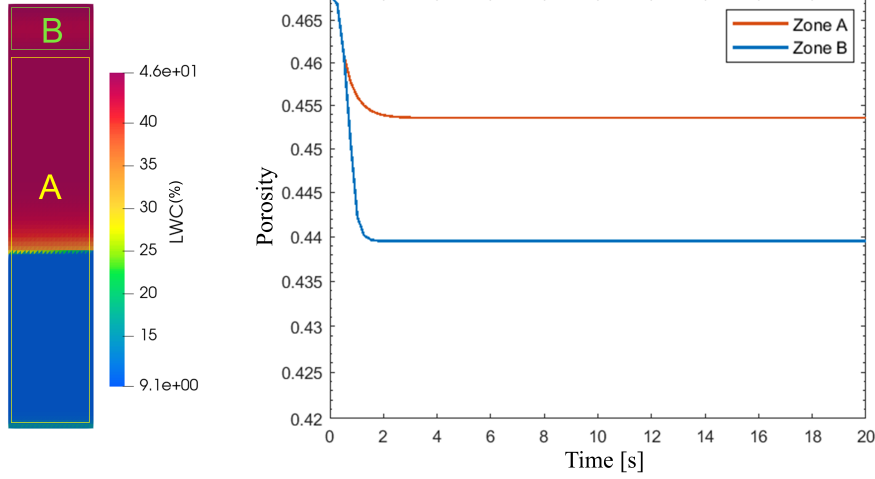
Figure 14: Temporal behaviour for averaged-Porosity ϕ on Zone A and Zone B.

As previously noted, the temperature of the ice approaches the melting point during the initial time period, owing to the heat released by the substantial presence of water within the domain. However, the process unfolds gradually. As shown in Figure 15, which plots the interface temperature against z for various time steps, we notice an undershoot in the interface temperature before reaching equilibrium. This undershoot is notably located at the infiltration front, due to the presence of relatively cold ice just beneath the front. Over time, we witness a decrease in both the intensity and quota of the undershoot. Note that this phenomenon is correlated with the variation of porosity in the same area.

In regions where the medium is completely saturated with water, the interface temperature reaches the melting point more rapidly than in the rest of the domain. The plot on the right side in Figure 15 provides a more detailed view of the interesting region in the left-hand plot.
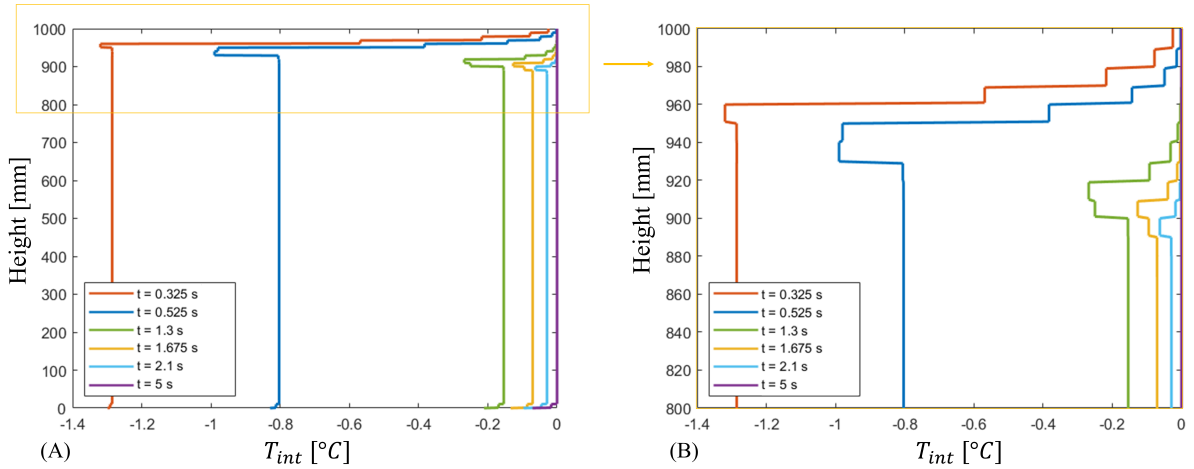
Figure 15: T_{int} profile along the vertical axis at various time instants. (B) provides a closer view for (A).

The immediate region closest to the ground ($z \to 0$) exhibits an interface temperature that approaches zero, yet never quite reaches the melting point, as depicted in Figure 15. In scenarios characterized by high saturations within the domain, the abundance of water prevents the lower layer from maintaining a cold environment. Following these considerations, opting for the Dirichlet condition $T_i = -5°\text{C}$ on Γ_b in the case of initial relatively wet snowpack might not be the optimal choice. In this context, imposing no temperature flux at the bottom boundary Γ_b may be more appropriate. Anyway, this setup is left for further developments.

Finally, the results regarding the iteration count for both the j-cycle and the k-cycle align with those of the previous test. Similarly, for the plot depicted in Figure 16(a), the time axis has been truncated, since from time step #190 the j-cycle stabilizes with a consistent number of iterations, settling at 2. As shown in Figure 16(b), the number of iterations for the Richards' nonlinear solver is high during the initial j-iterations corresponding to the initial time steps. The number of k-iterations settles to one iteration as the j-loop progresses.
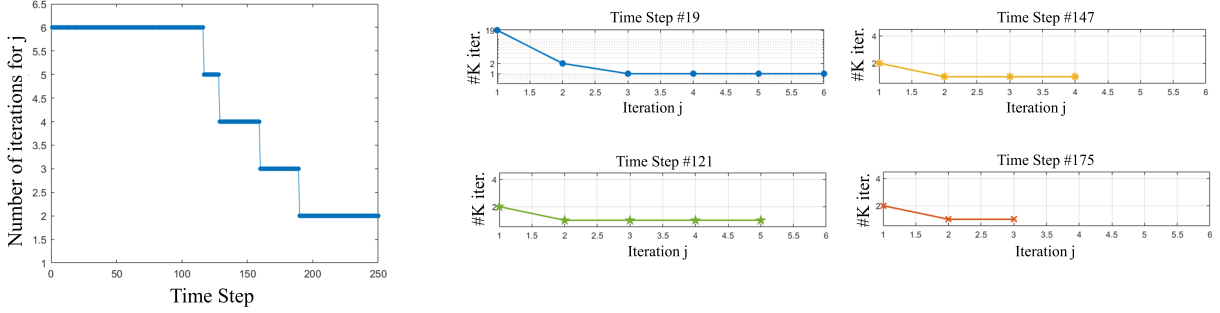
((a)) Number of iterations for the j-cycle per time step.

((b)) Number of iterations for the k-cycle per iteration j for four selected time steps.

Figure 16: Iteration count for Test Case 2.

5.4. Test Case 3: Infiltration with Non-Uniform External Pressure Distribution

In this section, we explore the model under two different setups with regard to the external source of pressure, and consequently, saturation. The characteristics of the two scenarios are as follows:

- Test Case 3/A involves a non-uniform water source from above: the natural boundary condition for ψ at the top is no longer uniform along Γ_t.
- Test Case 3/B examines the introduction of an instantaneous water injection, where a positive water source is injected exclusively within the domain at the initial time.

For these tests, we enforce the same initial conditions as in Test Case 2, namely, $\psi_0 = -0.22$ m, $\phi_0 = 0.468$, $T_{i,0} = -5°$C, and $T_{w,0} = 0°$C. An initially wet snowpack is thus considered. The boundary conditions for flux and thermodynamics remain unchanged, and the overall simulation length is $T = 118$ s with $\Delta t = 0.025$ s. Any modifications to the setup are explicitly stated for each test.

5.4.1 Test Case 3/A: Discrete source from above

The following test aims to assess the behavior of infiltration in the presence of a non-uniform water source at the top boundary.

As mentioned earlier, the numerical setup remains consistent with Test Case 2. Here, the only variation occurs in the condition along Γ_t. Specifically, we have:

$$\psi_{top}(x) = \begin{cases} 1 & \text{if } x \in \Gamma_t^A \\ 0 & \text{if } x \in \Gamma_t^B \end{cases}$$

where

$$\Gamma_t^A = \{(x,z) \in \Gamma_t \,|\, x \in [0.04, 0.06] \vee [0.14, 0.16]\},$$
$$\Gamma_t^B = \{(x,z) \in \Gamma_t \,|\, x \in [0, 0.04] \vee [0.06, 0.14] \vee [0.16, 0.2]\}$$

and $\Gamma_t = \Gamma_t^A \cup \Gamma_t^B$.

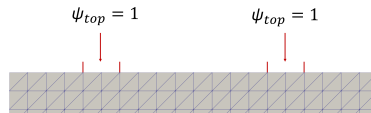The graphical representation of the new boundary condition is depicted in Figure 17:

Figure 17: New configuration for pressure at the top.

The infiltration dynamics is depicted in Figure 18. Upon the entry of water into the domain, infiltration not only proceeds vertically but also exhibits a horizontal component, saturating the domain in its width within the initial centimeters. Remarkably, at the abscissa where the source is located, the infiltration process is more developed. However, as time progresses, the profile of the front gradually loses its distinctive shape. It begins

30

to assume a more uniform appearance, indicating the beginning of a uniformly advancing infiltration process, approximately after $t = 25$ s.

The same line of reasoning to that used in Test Case 2 for temperatures and phase change can be applied in this scenario, with the only distinction being the source's distribution. Specifically, Figure 18.B reveals an undershoot in porosity, spatially manifested just beneath the surface, mirroring the shape of the profile of the infiltration front. The origin of this undershoot, attributed to thermodynamic processes, has already been explained in Section 5.3.
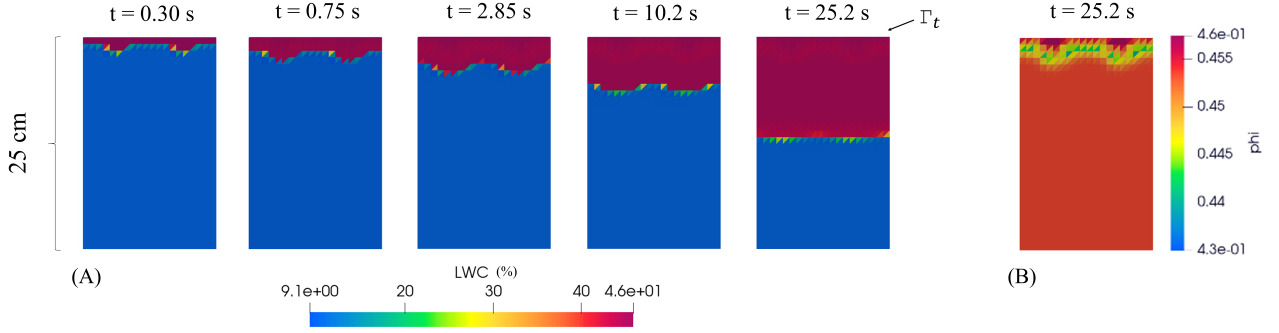
Figure 18: Discrete source at Γ_t. (A) LWC for four time instants, (B) Porosity for one time instant.

In the end, the outcomes regarding the iteration count for both the j-cycle and the k-cycle exhibit partial alignment with those observed in the previous analysis. Specifically, during the initial phases of the simulation, thermodynamics requires numerous iterations for convergence. However, starting from Time Step #5, the behavior closely corresponds to that observed in Test Case 2.
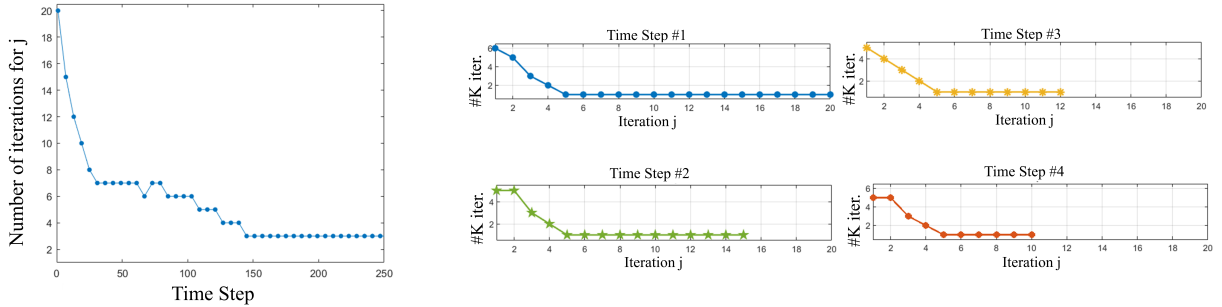
((a)) Number of iterations for the j-cycle per time step.

((b)) Number of iterations for the k-cycle per iteration j for four selected time steps.

Figure 19: Iteration count for Test Case 3/A.

5.4.2 Test Case 3/B: Instantaneous injection

In this section, the same identical numerical setup adopted in Section 5.3 is employed. In particular, uniform boundary condition for ψ is recovered, resulting in $\psi_{top} = 1$ across the entire Γ_t.

Here, we aim to evaluate the outcomes when subjecting our system to an instantaneous injection of water at $0°C$ within the domain. When dealing with "instantaneous" injection, we are referring to an operation that spans a single time step, which is equivalent to $\Delta t = 0.025$ seconds.

Additionally, we identify the specific region Ω^{inj} where the injection takes place:

$$\Omega^{inj} = \left\{ (x, z) \in \Omega \,|\, x \in [0.075, 0.125] \wedge z \in [0.45, 0.55] \right\}.$$

Hence, it should not be perceived as a point injection but it rather encompasses a broader area.

This phenomenon is modeled by introducing a positive source term into water mass conservation equation. With this adjustment, the continuous version of Equation (17) transforms into:

$$\rho_w \left(\frac{\partial \theta(\psi)}{\partial t} + \boldsymbol{\nabla} \cdot \mathbf{q} \right) = \rho_i R_m W_{SSA}(T_{int} - T_{melt}) + f^{inj} \tag{63}$$

where, in this instance, we opted for $f^{inj} = 20$.

31

In the context of discretization, managing a constant source term presents no real challenges, as it remains on the right-hand side.

Figure 20.A illustrates the outcomes related to infiltration following the injection at time $t = 0$ s across the entire snowpack, along with the regular infiltration from above. While uniform infiltration has been previously examined in Test Case 2 (see Section 5.3), it is now interesting to observe the dynamics of the additional saturation introduced as a *bubble* in the middle of the domain. It's evident that, under the influence of gravity, the bubble begins its downward motion. However, its movement is not restricted to the vertical direction; it also displays a notable diffusive behavior, as discussed in Test Case 3/A (see Section 5.4.1). The infiltration velocity of the extra saturation is comparatively slower than that originating from above, indeed the instantaneous nature of its introduction prevents it from being propelled by a perpetual pressure. In addition, we can note that, especially from the early stages of the process, water descending from the upper region of the domain, under the influence of gravity, progressively gathers above the initial bubble.
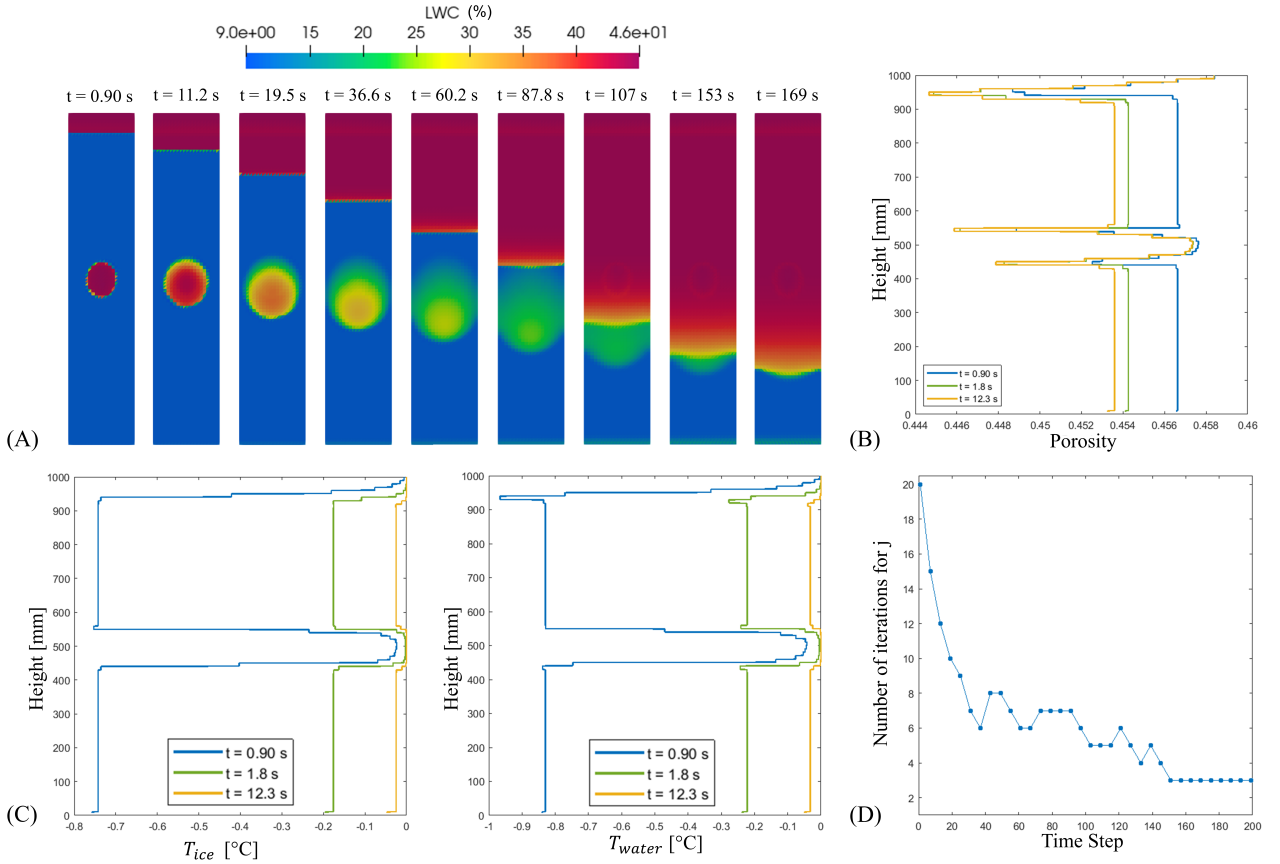The last steps of the simulation show the merging of the two infiltration fronts.

Figure 20: Instantaneous Injection. (A) LWC, (B) Porosity against height, (C) Ice and water temperatures against z, (D) Iteration count for the j-cycle.

The porosity profile along the vertical central axis of the domain is depicted in Figure 20.B for three distinct time steps. Overall, it is noticeable that porosity experiences a decrease in every region of the domain, attributed to the process of refreezing. While we have already delved into the formation of the undershoot beneath the surface, it is worth noting that a similar phenomenon is observed at the interface between the region of the initial injection and the rest of the domain: in particular, in Figure 20.A, we can discern that LWC displays a memory effect associated with a lower value of porosity. Meanwhile, within the internally saturated region, it is evident that porosity attains its maximum value throughout the snowpack, where we excluded the cell directly beneath the surface. The instantaneous injection, initially endowed with a certain pressure, accelerates the ice approach to the melting point, limiting the refreezing in that area.

The simulated temperatures are illustrated in Figure 20.C. The ice undergoes rapid warming in the region where the injection occurs. Additionally, following cooling across all regions, water swiftly returns to 0°C. Certainly, the dynamics we've discussed is notably faster in regions with a higher water content.

Finally, Figure 20.D shows the number of iterations for the j-cycle at each time step, exhibiting behavior consistent with the previous test case. Again, the temporal representation horizon has been limited to time

step #200, beyond which the number of iterations stabilizes. In this instance, the number of iterations for the k-cycle for every j iteration is not reported, as it mirrors the behavior observed in the Test Case 3/A.

5.5.   Test Case 4: Grain Size-Induced Heterogeneous Infiltration

In this concluding section, we delve into a scenario where we introduce heterogeneities to the snowpack. In terms of boundary conditions, we maintain the same numerical setup as in the previous tests. Also the initial conditions are kept unchanged, in particular they read: $\psi_0 = -0.22$ m, $S_0 \approx 0.223$, $\phi_0 = 0.468$, $T_{i,0} = -5°$C, $T_{w,0} = 0°$C. The overall simulation length is $T = 230$ s with $\Delta t = 0.1$ s. What distinguishes this test from the previous ones is the incorporation of heterogeneities within the domain. This is achieved by introducing variations in the sizes of ice crystals in the snow. The new physical configuration is presented in Figure 21:
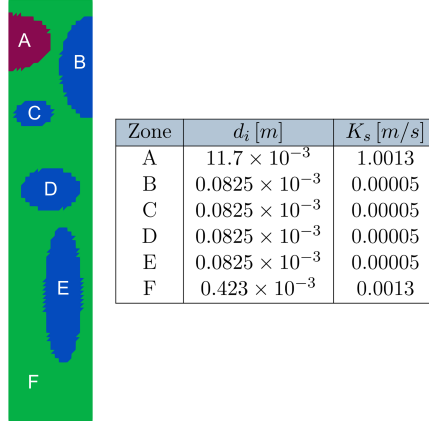

Zone	$d_i\,[m]$	$K_s\,[m/s]$
A	11.7×10^{-3}	1.0013
B	0.0825×10^{-3}	0.00005
C	0.0825×10^{-3}	0.00005
D	0.0825×10^{-3}	0.00005
E	0.0825×10^{-3}	0.00005
F	0.423×10^{-3}	0.0013

Figure 21: Scheme of the snowpack hetereogeneity.

where, for each zone in the domain, we also provided the corresponding absolute conductivity in the table on the right. Coherently with expression (21), we have that K_s is directly proportional to d_i. Naturally, as K_s increases, the overall permeability of the medium also rises.
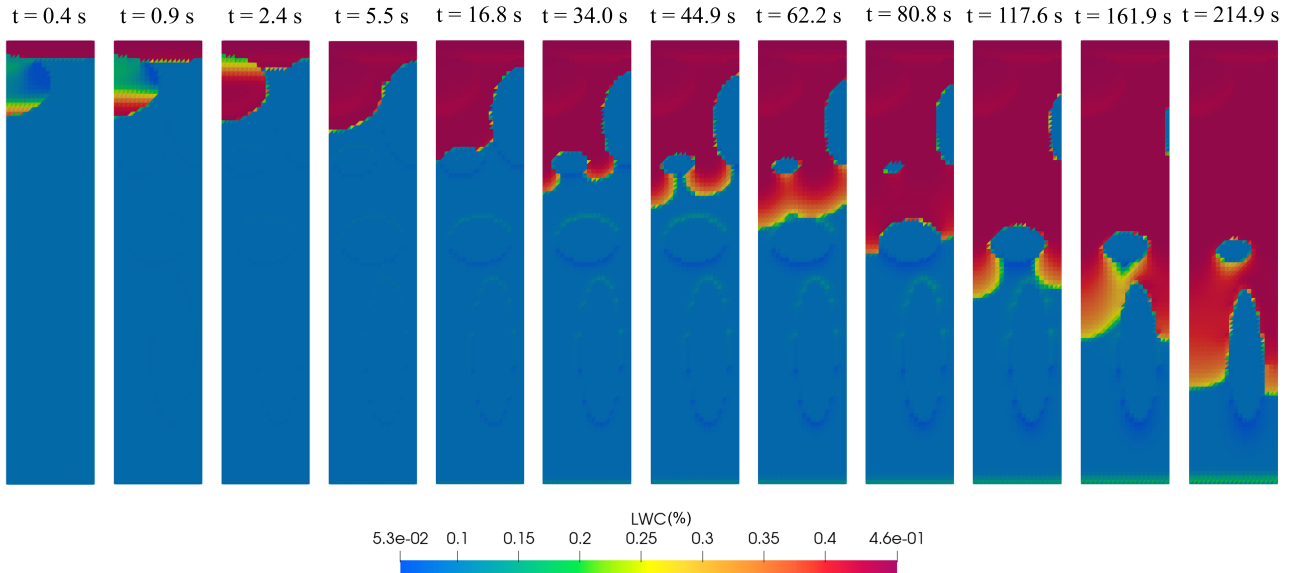The simulated infiltration is illustrated in Figure 22:

Figure 22: Grain Size-Induced Heterogeneous infiltration.

Especially remarkable is the tendency of water to follow paths characterized by higher permeability, as infiltration is facilitated in these areas. Conversely, regions with closer-to-impermeable characteristics tend to be initially avoided. Nevertheless, the less permeable zones are not completely impermeable; as time progresses, Zones B, C, D, E also reach full saturation. It's fascinating to observe how the liquid phase within the snowpack, guided by gravity, accumulates both over regions with low permeability and at the bottom of the snowpack. In

addition, in line with the analysis conducted in previous tests, we can observe in Figure 22 the memory effect of the refreezing process in the zones that initially achieved full saturation. This is indeed highlighted by the orange areas at the top of the snowpack, indicative of a lower porosity value.

Concerning temperatures, their behaviour is depicted in Figure 23, focusing on the initial 50 cm of the snowpack:
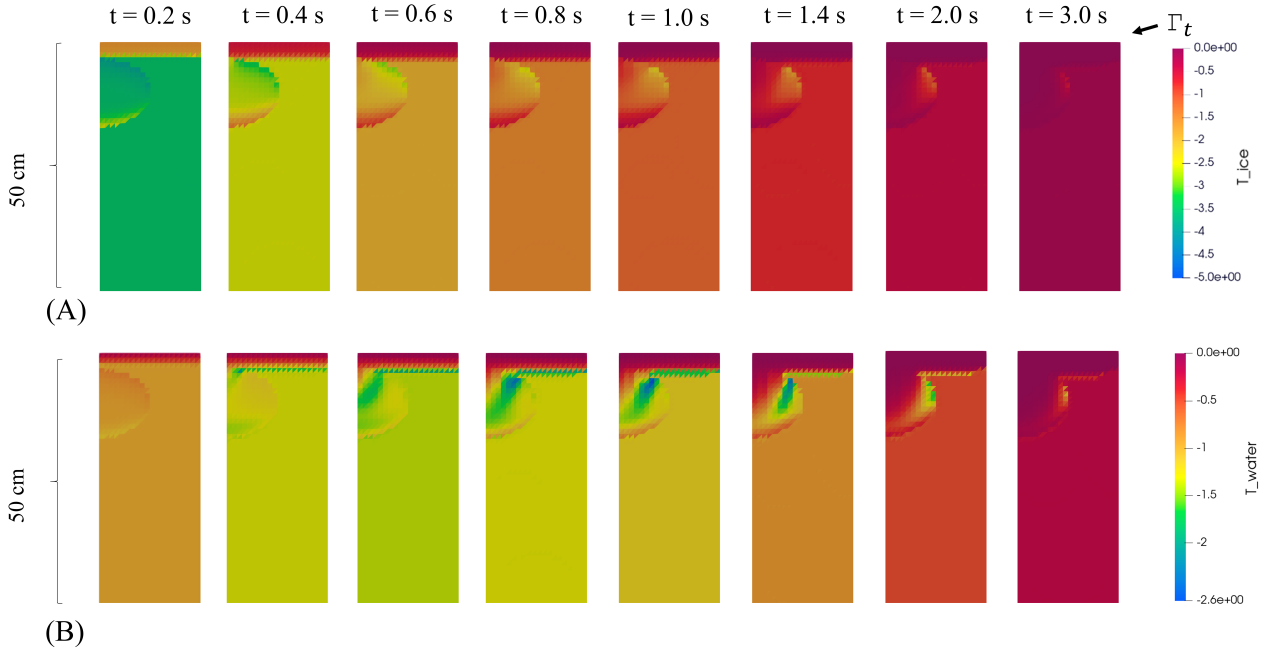

Figure 23: Grain Size-Induced Heterogeneous infiltration, Thermodynamics component. (A) T_i, (B) T_w.

Equilibrium is quickly achieved almost uniformly throughout the snowpack. Introducing a uniform porosity and saturation at $t = 0$ s ensures an initially homogeneous moisture content across the entire domain, however, variations in grain sizes play a role in the timing of the process. In Zone A, for example, a trade-off emerges between rapid heat exchange, facilitated by a sudden abundance of water, and a more gradual process due to the larger ice crystals constituting the solid matrix.

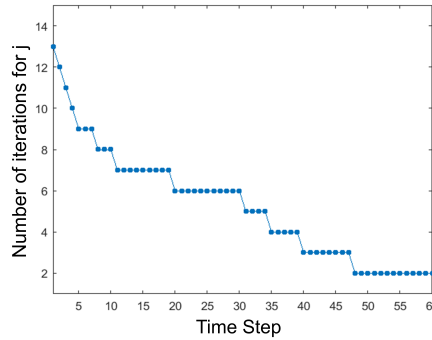Finally, the iteration count for the j-cycle is provided in Figure 24:

Figure 24: Test Case 4. Iteration count for the j-cycle.

where the plot undergoes temporal truncation. Starting from time step #48, the j-cycle consistently holds an iteration count of 2 for each subsequent time step.

6.   Conclusions and Future Developments

A challenging problem in hydrogeology involves modeling the transport of surface-generated meltwater into snow, which can be classified as a porous medium [18, 23, 33]. It represents a crucial element for assessing and mitigating the risk of avalanches and comprehending glacier movement. Infiltrating water can act, for instance, as a lubricant, facilitating the sliding of the snowpack or glacier over the underlying bedrock. Through detailed studies, the prediction of snow stability and glacier dynamics can be enhanced, providing a solid foundation for

34

the development of predictive models and early warning systems. These contributions are essential for public safety management, safeguarding water resources, and understanding the impacts of climate change on snowy and glacial landscapes.

To model and implement the phenomenon of flow of meltwater through snow, we developed an intricate iterative coupling strategy that manages the interplay between infiltration, regulated by Richards' equation, and thermodynamics, represented by advection-diffusion-reaction equations governing heat exchange and phase change processes. Regarding the latter, two equations have been formulated and implemented to track the temperature fields associated with water and ice [23]. After detailing every aspect of the model, we then derived the fully discretized versions of all the involved equations for numerical resolution. We finally performed several numerical tests to evaluate infiltration along with the thermodynamics associated with phase change, specifically solidification resulting from refreezing. In particular, we examined different physical setups to understand the nature of the phenomenon in varying conditions. Specifically, we noted that the initial dryness level of the snowpack has a pronounced impact on the speed and overall dynamics associated with the infiltration process. As mentioned in Section 3, an interesting approach to more accurately replicate the observed physical phenomenon, marked by preferential flow caused by gravity fingering instabilities, could be to incorporate an extension to Richards' equation, specifically a fourth-order term in saturation. This represents a substantial challenge from a numerical perspective but could lead to a significant advancement in the investigation of the transport of meltwater into snow, allowing us to model fingering.

Furthermore, in our model, we assume the density of ice to be constant from the outset, implying an incompressible snowpack. Introducing a law for density would add the property of compressibility to the domain, yielding even more realistic results. Moreover, it might be interesting to simulate and then compare the outcomes in the case of different grain sizes.

Numerically speaking, it might represent an interesting possible future development to refine the coupling and splitting strategy, which is currently outlined in Section 4.3.1, to achieve enhanced convergence efficiency. Currently, the Δt values employed are indeed quite small in comparison to the intended temporal horizon for simulations. Simultaneously, employing a time adaptivity approach could prove more advantageous in reducing the overall computational costs.

References

[1] A. Fumagalli A. Scotti. Notes of the course "numerical methods for the geosciences". 12 2023.

[2] Nagi Abdussamie. Flow and transport problems in porous media using cfd, 02 2014.

[3] Lucio Barbiero, Lisa Maria Castro Tellez, Angela Di Ruocco, and Domenico Pianese. Modellazione numerica, attraverso la tecnica dei volumi finiti, dei fenomeni di evoluzione d'alveo. Giornale di Geologia Applicata, 2:173–180, 2005.

[4] Sabrina Bassetto. Towards more robust and accurate computations of capillary effects in the simulation of multiphase flows in porous media. PhD thesis, Université de Lille, Rueil-Malmaison, 12 2021.

[5] Peter Bastian. Numerical Computation of Multiphase Flows in Porous Media. Christian-Albrechts-Universitat Kiel, Kiel, 1999.

[6] J. Bear and Y. Bachmat. Introduction to Modeling of Transport Phenomena in Porous Media. Theory and Applications of Transport in Porous Media. Springer Netherlands, 2012.

[7] N. Calonne, C. Geindreau, F. Flin, S. Morin, B. Lesaffre, S. Rolland du Roscoat, and P. Charrier. 3-d image-based numerical computations of snow permeability: links to specific surface area, density, and microstructural anisotropy. The Cryosphere, 6(5):939–951, 2012.

[8] Fay M. A. Campbell, Peter W. Nienow, and Ross S. Purves. Role of the supraglacial snowpack in mediating meltwater delivery to the glacier system as inferred from dye tracer investigations. Hydrological Processes, 20(4):969–985, 2006.

[9] Jerome Droniou. Finite volume schemes for diffusion equations: introduction to and review of modern methods. Mathematical Models and Methods in Applied Sciences, 24(08):1575–1619, 2014.

[10] Ricardo G. Duran. Mixed Finite Element Methods, volume 4. Springer, Berlin, Heidelberg, 7 2008.

[11] Alessio Fumagalli Anna Scotti Enrico Ballini, Wietse Boon. Pygeon: a python package for geo-numerics. url https://github.com/compgeo-mox/pygeon, 2022.

[12] Samantha L. Evans, Alejandro N. Flores, Achim Heilig, Matthew J. Kohn, Hans-Peter Marshall, and James P. McNamara. Isotopic evidence for lateral flow and diffusive transport, but not sublimation, in a sloped seasonal snowpack, idaho, usa. Geophysical Research Letters, 43(7):3298–3306, 2016.

[13] Gabriel Gatica. A Simple Introduction to the Mixed Finite Element Method. Theory and Applications. 01 2014.

[14] B. GHANBARIAN-ALAVIJEH, A. LIAGHAT, Guan-Hua HUANG, and M. Th. VAN GENUCHTEN. Estimation of the van genuchten soil water retention properties from soil textural data. Pedosphere, 20(4):456–465, 2010.

[15] Hector Gomez, Miguel Bures, and Adrian Moure. A review on computational modelling of phase-transition problems. Philosophical Transactions of the Royal Society A: Mathematical, Physical and Engineering Sciences, 377(2143):20180203, 2019.

[16] T Heinze. A multi-phase heat transfer model for water infiltration into frozen soil. Water Resources Research, 57(10):e2021WR030067, 2021.

[17] M. King Hubbert. Darcy's Law and the Field Equations of the Flow of Underground Fluids. Transactions of the AIME, 207(01):222–239, 12 1956.

[18] Takafumi Katsushima, Satoru Yamaguchi, Toshiro Kumakura, and Atsushi Sato. Experimental analysis of preferential flow in dry snowpack. Cold Regions Science and Technology, 85:206–216, 2013.

[19] Berge R. Fumagalli A. Starnoni M. Stefansson I. Varela J. Berre I. Keilegavlen, E. Porepy: an open-source software for simulation of multiphysics processes in fractured porous media. Computational Geosciences, 25:243–265, 10 2021.

[20] A. Koponen, M. Kataja, and J. Timonen. Permeability and effective porosity of porous media. Phys. Rev. E, 56:3319–3325, Sep 1997.

[21] R.J. LeVeque. Finite Volume Methods for Hyperbolic Problems. Cambridge Texts in Applied Mathematics. Cambridge University Press, 2002.

[22] Florian List and Florin A Radu. A study on iterative methods for solving richards' equation. Computational Geosciences, 20:341–353, 2016.

[23] Adrian Moure, Nathan Jones, Joshua Pawlak, Colin Meyer, and Xiaojing Fu. A thermodynamic nonequilibrium model for preferential infiltration and refreezing of melt in snow. Water Resources Research, 59(5):e2022WR034035, 2023. e2022WR034035 2022WR034035.

[24] Yechezkel Mualem. A new model for predicting the hydraulic conductivity of unsaturated porous media. Water Resources Research, 12(3):513–522, 1976.

[25] G.F. Pinder and M.A. Celia. Subsurface Hydrology. Wiley, 2006.

[26] Iuliu Sorin Pop, FLORIN Radu, and Peter Knabner. Mixed finite elements for the richards' equation: linearization procedure. Journal of computational and applied mathematics, 168(1-2):365–373, 2004.

[27] Alfio Quarteroni. Numerical Models for Differential Problems, volume 1. Springer Milano, 2 edition, 4 2014.

[28] L. A. Richards. CAPILLARY CONDUCTION OF LIQUIDS THROUGH POROUS MEDIUMS. Physics, 1(5):318–333, 11 1931.

[29] Nicolae Suciu, Florin A Radu, Jakob S Stokke, Emil Cătinaş, and Andra Malina. Computational orders of convergence of iterative methods for richards' equation. arXiv preprint arXiv:2402.00194, 2024.

[30] Nicolae Suciu, Florin A Radu, Jakob S Stokke, Emil Cătinaş, and Andra Malina. Computational orders of convergence of iterative methods for richards' equation. arXiv preprint arXiv:2402.00194, 2024.

[31] Vidar Thomée. Galerkin finite element methods for parabolic problems, volume 25. Springer Science & Business Media, 2007.

[32] M. Th. van Genuchten. A closed-form equation for predicting the hydraulic conductivity of unsaturated soils. Soil Science Society of America Journal, 44(5):892–898, 1980.

[33] R. W. Webb, K. Jennings, S. Finsterle, and S. R. Fassnacht. Two-dimensional liquid water flow through snow at the plot scale in continental snowpacks: simulations and field data comparisons. The Cryosphere, 15(3):1423–1434, 2021.

[34] Satoru Yamaguchi, Kunio Watanabe, Takafumi Katsushima, Atsushi Sato, and Toshiro Kumakura. Dependence of the water retention curve of snow on snow characteristics. Annals of Glaciology, 53(61):6–12, 2012.

A.   Appendix A

The purpose of this section is to formulate the mass balance equation for a porous medium. Starting from the usual mass conservation equation for a domain Ω, the mass conservation equation in the case of porous medium can be rewritten as:

$$\int_V \frac{1}{|REV(\mathbf{x},t)|} \int_{REV(\mathbf{x},t)} \left(\frac{\partial \rho}{\partial t} - \tilde{f} + \boldsymbol{\nabla} \cdot (\rho \mathbf{v}) \right) \gamma_l(\mathbf{x}+\boldsymbol{\xi},t) dv_\xi dV = 0, \tag{64}$$

with

$$\gamma_\alpha(\mathbf{r},t) = \begin{cases} 1 & \text{if } \mathbf{r} \in V_l, \\ 0 & \text{if } \mathbf{r} \in V_s. \end{cases}$$

where $\mathbf{r} = \mathbf{x}+\boldsymbol{\xi}$, with $\mathbf{x}$ being the center of the REV and $\boldsymbol{\xi}$ the local coordinate of the point relative to $\mathbf{x}$. Here, V_α represents the region occupied by phase α.

Since the functional form of γ_l is unknown, a practically useful approach is to employ the *volume average* $\langle \cdot \rangle_\alpha(\mathbf{x},t)$ tool:

$$\langle \cdot \rangle_\alpha(\mathbf{x},t) := \frac{1}{|REV(\mathbf{x},t)|} \int_{REV(\mathbf{x},t)} (\cdot)(\mathbf{x}+\boldsymbol{\xi},t) \gamma_\alpha(\mathbf{x}+\boldsymbol{\xi},t) dv_\xi, \tag{65}$$

Essentially, the characteristics associated with pore size, shape, and distribution have been incorporated into the overall average through the process of integration.

By combining Equation (4) and Equation (65) we get, for the fluid phase:

$$\int_V \left\langle \frac{\partial \rho}{\partial t} + \tilde{f} + \boldsymbol{\nabla} \cdot (\rho \mathbf{v}) \right\rangle_l dV = 0, \tag{66}$$

Now, in the context of a single-phase fluid where no phase change can occur, and recognizing the arbitrariness of the volume V, Equation (66) can be reformulated as:

$$\frac{\langle \partial \rho \rangle_l}{\partial t} + \boldsymbol{\nabla} \cdot \left(\langle \rho \rangle_l \overline{(\mathbf{v})}^l \right) = \langle \tilde{f} \rangle_l. \tag{67}$$

where

$$\overline{(\cdot)}^\alpha(\mathbf{x},t) := \frac{1}{\langle \rho \rangle_l(\mathbf{x},t)|REV(\mathbf{x},t)|} \int_{dV REV(\mathbf{x},t)} \rho(\mathbf{x}+\boldsymbol{\xi},t)(\cdot)(\mathbf{x}+\boldsymbol{\xi},t)\gamma_l(\mathbf{x}+\boldsymbol{\xi},t) dv_\xi.$$

The detailed calculations are presented in [25].

The nature of $\langle \rho \rangle_l$, however, is ambiguous, as it is given by the ratio between the mass of the fluid and the volume of both solid and liquid phases. In order to give to Equation (67) a physical meaning, let us introduce the *intrinsic volume average*, $\langle \cdot \rangle_\alpha^\alpha(\mathbf{x},t)$, defined as

$$\langle \cdot \rangle_\alpha^\alpha(\mathbf{x},t) := \frac{1}{\int_{REV(\mathbf{x},t)} \gamma_\alpha dV} \int_{REV(\mathbf{x},t)} (\cdot)(\mathbf{x}+\boldsymbol{\xi},t)\gamma_\alpha(\mathbf{x}+\boldsymbol{x i},t) dv_\xi, \tag{68}$$

We can easily notice that $\langle \cdot \rangle_l = \phi \langle \cdot \rangle_l^l$, where ϕ is the porosity. By combining Equation (67) with Equation (68) we obtain

$$\frac{\partial \phi \langle \rho \rangle_l^l}{\partial t} + \boldsymbol{\nabla} \cdot \left(\phi \langle \rho \rangle_l^l \overline{(\mathbf{v})}^l \right) = \phi \langle \tilde{f} \rangle_l^l.$$

that is the mass conservation equation for a single-fluid in a porous medium.

The notation can be simplified by writing

$$\frac{\partial(\phi\rho)}{\partial t} + \boldsymbol{\nabla} \cdot (\phi\rho\mathbf{v}) = f \tag{69}$$

where $f = \phi\langle\tilde{f}\rangle_l^l$ and it is important to remember that we are dealing with averaged quantities.

B. Appendix B

The equations characterizing the zero-dimensional system, the outcomes of which are examined in Section 5.1, are presented below:

$$
\begin{cases}
\rho_i \dfrac{\partial(1-\phi)}{\partial t} = -\rho_i R_m W_{SSA}(T_{int} - T_{melt}) & \text{(70a)} \\[2mm]
\rho_w \dfrac{\partial(\phi S)}{\partial t} = \rho_i R_m W_{SSA}(T_{int} - T_{melt}) & \text{(70b)} \\[2mm]
\rho_i c_i \dfrac{\partial[(1-\phi)T_i]}{\partial t} = -\alpha_i \rho L_{sol} R_m W_{SSA}(T_{int} - T_{melt}) & \text{(70c)} \\[2mm]
\rho_w c_w \dfrac{\partial(\phi S T_w)}{\partial t} = -\alpha_w \rho L_{sol} R_m W_{SSA}(T_{int} - T_{melt}) & \text{(70d)}
\end{cases}
$$

where the selection of ρ is contingent upon the direction of the phase change process. For the sake of simplicity, we assume here that $\rho = \rho_w$.

As the domain is characterized by one single cell, no space discretization is needed. On the other hand, the temporal discretization is accomplished using the Backward Euler method. Let $(0, T)$ denote the entire time span of interest, N_{ts} be the number of time steps such that the single time step has a temporal length of $\Delta t = T/N_{ts}$. A discrete sequence of time instants can be defined $\{t_n\}_{n=0}^{N_{ts}}$ such that $t_{n+1} = t_n + \Delta t$. The discretized problem reads as follows:

Given $(\phi_0, S_0, T_{i,0}, T_{w,0})$, *find* $\forall n = 0, ..., N_{ts} - 1$ $(\phi^{n+1}, S^{n+1}, T_{i,0}^{n+1}, T_{w0}^{n+1})$ *such that:*

$$
\begin{cases}
\phi^{n+1} = \phi^n + \Delta t f_1(\phi^{n+1}, S^{n+1}, T_i^{n+1}, T_w^{n+1}) & \text{(71a)} \\[2mm]
S^{n+1} = S^n + \Delta t f_2(\phi^{n+1}, S^{n+1}, T_i^{n+1}, T_w^{n+1}) & \text{(71b)} \\[2mm]
T_i^{n+1} = T_i^n + \Delta t f_3(\phi^{n+1}, S^{n+1}, T_i^{n+1}, T_w^{n+1}) & \text{(71c)} \\[2mm]
T_w^{n+1} = T_w + \Delta t f_4(\phi^{n+1}, S^{n+1}, T_i^{n+1}, T_w^{n+1}) & \text{(71d)}
\end{cases}
$$

where f_1, f_2, f_3, f_4 are appropriate functions that can be readily derived by following the structure of the equations in System 70.

Abstract in lingua italiana

Il fenomeno del trasporto dell'acqua di disgelo attraverso la neve, classificata come un mezzo poroso, rappresenta un processo idrologico essenziale per prevedere la risposta della criosfera ai cambiamenti climatici. Questa tesi si propone di modellare l'interazione complessa tra l'infiltrazione dell'acqua di disgelo e le dinamiche di cambio di fase tra acqua e ghiaccio, generate da una condizione fisica di disequilibrio tra le due fasi. Il modello proposto incorpora l'equazione di Richards per l'infiltrazione, insieme a due equazioni di evoluzione che governano i campi di temperatura per la fase solida e liquida e il bilancio termico del manto nevoso. Inoltre, il modello tiene conto delle variazioni nella porosità. Questo studio presenta risultati numerici derivanti da simulazioni condotte su modelli 2D di manti nevosi con diversi livelli iniziali di umidità e differenti configurazioni fisiche, i quali esaminano la meccanica dell'infiltrazione e dell'alterazione della struttura di porosità a causa del processo di solidificazione dell'acqua all'interno del manto nevoso. L'implementazione fa uso delle librerie Python *PorePy* e *PyGeoN*.

Parole chiave: equazione di richards; acqua di disgelo; congelamento; infiltrazione; cambio di fase; metodo degli elementi finiti misti; metodo dei volumi finiti